

ADVANCED MODELING AND ANALYSIS OF A LIQUID HYDROGEN SHORT-MEDIUM RANGE AIRCRAFT CONCEPT FOR 2035

Michael Kotzem[1], Jannik Häßy[2], Vivian Kriewall Peters[3], Paul Schatrow[4] & Sebastian Wöhler[1]

[1]German Aerospace Center (DLR), Institute of System Architectures in Aeronautics, Hamburg, 21129, Germany
[2]German Aerospace Center (DLR), Institute of Propulsion Technology, Cologne, 51147, Germany
[3]Hamburg University of Technology (TUHH), Institute of Aircraft Systems Engineering, Hamburg, 21129, Germany
[4]German Aerospace Center (DLR), Institute of Structure and Design, Stuttgart, 70569, Germany

Abstract

The integration of liquid hydrogen (LH_2) as an energy carrier leads to unconventional fuel storage concepts, resulting in higher uncertainties during the conceptual design phase compared to kerosene fueled aircraft concepts. Due to the novelty of LH_2 powered aircraft designs, there is a lack of empirical data and established methodologies, which often necessitates a reliance on technical assumptions across various disciplines. Consequently, the present study focuses on the maturation of an existing LH_2 aircraft design featuring a caudal tank integration concept, which has been identified in prior research as the most favourable configuration. The maturation is achieved by employing detailed component design studies and higher-fidelity simulations and subsequently integrating the findings into the overall aircraft design process. The on-board and hydrogen system architecture is derived, including a detailed system topology. Additionally, an engine model specifically designed for hydrogen combustion considering the pre-conditioning of hydrogen is integrated. For the structural integration of the hydrogen tanks, an initial crash concept is developed and crash simulations are carried out for selected crash cases to validate the concept. Furthermore, the updated LH_2 aircraft is compared with its previous iteration and a technologically equivalent aircraft powered by sustainable aviation fuel (SAF). The results indicate that the engine mass is lower than previously assumed and mid-cruise thrust-specific energy consumption shows a deviation from initial expectations, yet still demonstrates an improvement over the engine of the SAF aircraft. Furthermore, the detailed component design studies reveal an increase in mass for the hydrogen systems as well as an increase of the fuselage mass penalty for the integration of the LH_2 tanks and associated crash concepts. Overall, the mission efficiency of the revised LH_2 aircraft design is increased compared to its previous version.

Keywords: Overall Aircraft Design, Hydrogen Aircraft, Propulsion Technology, System Design, Crashworthiness

1. Introduction

In order to mitigate the environmental impact of the aviation sector and achieve long-term climate targets [1], liquid hydrogen (LH_2) has emerged as a promising energy carrier. The application of LH_2 in aviation raises new challenges for the aircraft design process. The low volumetric energy density of LH_2 demands cryogenic storage conditions, significantly increasing the complexity of tank integration within the aircraft. Consequently, unconventional tank integration concepts must be employed, resulting in substantial alterations to the common aircraft design of tube and wing configurations. These alterations fundamentally challenge the conventional aircraft conceptual design process, which relies predominantly on empirical handbook methods whose validity is rooted in the extensive data of conventional, kerosene fueled aircraft.

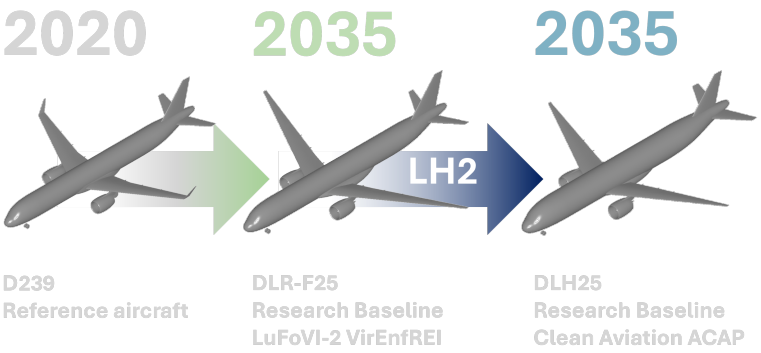
Current conceptual overall aircraft design studies on LH_2 aircraft configurations [2, 3, 4, 5, 6, 7, 8, 9] continue to utilise these established methodologies, supplementing them with specific technological assumptions specified for LH_2 aircraft design. For instance, divergent approaches are observed regarding mass estimations. While [2] assumes a mass penalty for the structural integration of the LH_2 tanks, [5] assumes that the fuselage mass remains constant, as the additional structural mass is offset by the removal of secondary structures in the tank region. Furthermore, although [6] sizes the tank integration structure based on regulatory loads for emergency landing conditions, the impact on the overall fuselage mass due to structural reinforcement is not considered, nor is the structural layout validated through dedicated crash simulations. Similarly, the treatment of propulsion efficiency for the substitution of kerosene by hydrogen varies. In [7] an additional reduction factor for specific fuel consumption (SFC) of 4.3% based on Brewer [10] is applied to the utilised hydrogen engine model, while in [8] the gas turbine efficiency is assumed to increase by 3.0%, and [9] scales the fuel consumption based on the difference in fuel calorific values between kerosene and hydrogen.
Parallel to these conceptual studies, significant progress has been made in detailed research focusing on individual components. Detailed studies have advanced the maturation of cryogenic tanks modeling [11, 12], thermodynamic characteristics [13, 14], thermal insulation [15], and combustion systems [16, 17, 18]. Due to the highly interconnected nature of aircraft design, detailed results at the component level inevitably have an impact on the overall aircraft and its performance. Consequently, it is essential to systematically integrate these refined findings into the conceptual design in order to replace initial technical assumptions. This integration is of particular value in establishing a research baseline, as such a reference point serves as the foundation for numerous subsequent studies.
In a preceding study [19], the author derived a LH_2 research baseline for the short-medium range segment (DLH25) from a research baseline powered by sustainable aviation fuel (SAF) [20]. In view of the absence of design methodologies and established empirical data for LH_2 powered aircraft, the initial derivation of the baseline was necessarily dependent on a substantial number of technical assumptions and approximations, particularly with regard to system masses, structural integration effects, and engine performance. The present study extends the DLH25 research baseline by increasing its level of maturity. The objective is to evolve the baseline from a conceptual framework into a more refined and detailed reference point by effectively replacing specific technological assumptions with more sophisticated simulation results, detailed component studies and more rigorous constraints. By substituting these assumptions with enhanced data, a more critical revision of the aircraft configuration can be performed, allowing for a detailed comparison between the initial assumptions and the refined design. This includes the integration of a detailed on-board system architecture that includes the hydrogen fuel-systems and a detailed system topology. Closely related is the integration of an ultra high bypass ratio turbofan engine that has been designed for the combustion of LH_2 and also considers the pre-conditioning of hydrogen. Moreover, the framework for integrating diverse crash concepts into the DLH25 is established. This framework encompasses the structural integration of an initial crash concept for the LH_2 tanks, which is executed on the basis of specific crash scenarios and analysed through the utilisation of high-fidelity crash simulations. The corresponding results of these higher-fidelity findings are finally integrated into the DLH25 research baseline and compared to the previous assumptions.
The remainder of this paper is structured as follows: Following the introduction, the methodology for the multidisciplinary and multifidelity aircraft design workflow is detailed. This section includes the interface to the detailed component design studies, as well as the methodology for the studies themselves, specifically covering the on-board LH_2 system architecture, the LH_2 engine design, and the crashworthy structural integration of the LH_2 tanks. Chapter 3 presents the corresponding results of these detailed component design studies. In Chapter 4, the initial assumptions are compared with the updated results derived from the detailed studies. These results are then integrated into the overall aircraft design, and the DLH25 is compared to both its predecessor and a technologically equivalent SAF powered aircraft. Finally, Chapter 5 concludes the paper with a summary of the findings and an outlook for future work.

2. Methodology

For the overall aircraft design, an established, multidisciplinary and multifidelity design workflow is employed [21]. This workflow is capable of ingesting results from the component design studies as inputs and, accordingly, adjusting the entire hydrogen aircraft design. Due to its extensive parametrization, rapid iterations can be performed using multifidelity data, feeding the revised concept back into the component studies until a converged solution is achieved.

2.1 Overall Aircraft Design

The foundation for the overall aircraft design process consists of the Top-Level Aircraft Requirements (TLARs) and the D239 reference configuration, a conventional short-medium range aircraft concept reflecting a 2020 technology level. This configuration served as the reference aircraft for the development of the SAF research baseline DLR-F25 including a 2035 technology level, which in turn provides the framework for the LH_2 research baseline DLH25. While the most critical TLARs are presented in Figure 1 next to the three aircraft designs, detailed specifications of the TLARs, the D239, and the resulting DLR-F25 SAF research baseline are documented in [20]. The present study adopts the DLH25 concept, as derived in [19], as its initial baseline. The DLH25 is characterized by a conventional tube-and-wing architecture, incorporating a low-wing arrangement and under-wing mounted ultra-high bypass ratio (UHBR) turbofan engines. To facilitate the integration of LH_2 tanks within the aft fuselage, the fuselage length and cross-section have been increased relative to the reference configuration. Additionally, the high aspect ratio of the wing, including a swept trailing edge at the kink, necessitates the implementation of a body-mounted landing gear.



Parameter	Value
Design Range	2500 NM
Design PAX	239
Mass per PAX	95 kg
Design Payload	25000 kg
Mach Cruise	0.78
Approach Speed	136 kts

Figure 1 – Aircraft concepts D239, DLR-F25 and DLH25 and key TLARs

The DLR's internal iterative, multidisciplinary and multifidelity overall aircraft design workflow has been established using the Remote Control Environment [22] framework and is depicted in Figure 2. Tools from different DLR institutes are integrated to incorporate various specialist disciplines in the design process. The CPACS schema is used as the interface for data exchange between the various tools [23]. A comprehensive description of the process is available in [19], encompassing detailed elaborations on each individual tool.

The result of the multidisciplinary and multifidelity aircraft design process is a CPACS dataset containing the initial aircraft geometry, component masses, center of gravity (CoG) positions, as well as aerodynamic and engine performance characteristics. This dataset serves as the starting point for the subsequent component design studies. The aircraft geometry defines the available spatial boundaries for the integration of the on-board and LH_2 system architectures, as well as geometric installation space in the tank mounting area for the crash concept. Initial engine performance is represented by an engine performance map, which resolves engine specific performance parameters, specifically thrust and fuel mass flow, as functions of Mach number and altitude. The design of the LH_2 engine, considering the required heat flows for LH_2 pre-conditioning, is predominantly dictated by the thrust requirements derived from the initial aircraft design, in addition to the off-take requirements that emerge from the on-board system architecture design. In addition to the thrust requirements, the sensitivities to changes in engine geometry, mass and specific fuel consumption relative to block

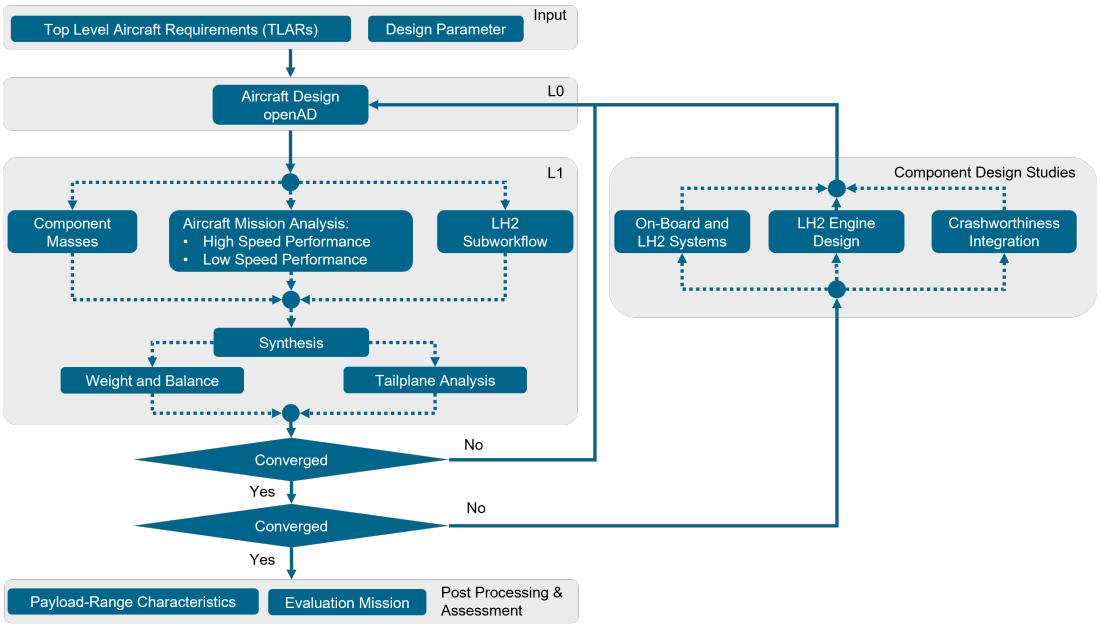


Figure 2 – Multidisciplinary and multifidelity overall aircraft design (OAD) workflow including the component design studies

energy consumption are determined for the LH_2 engine design. The results of the component design studies are subsequently fed back and integrated into the aircraft design loop. Specifically, the respective component masses, CoG positions and spatial requirements for the on-board and LH_2 systems architecture, as well as the crash structure, derived from the high-fidelity simulations are incorporated. The engine mass and geometry is updated and the initial low-fidelity performance map is replaced by the engine performance map resulting from the component design.

2.2 On-Board and LH_2 System Design

For the conceptual design of relevant on-board and LH_2 systems, the Overall System Design (OSD) framework developed by the Institute of Aircraft Systems Engineering at the Hamburg University of Technology is employed [20, 24, 25, 26]. It provides methodologies to conduct comprehensive design studies and analyses of on-board system (OBS) architectures based on physics-based sizing routines. Central to this approach is the integration of the CPACS interface [23, 27], which enables the import of relevant parameters from the OAD process. The OBS sizing results, such as masses, center of gravity positions, and engine power off-takes, are fed back to seamlessly close the overall aircraft design loop [28].

Based on the imported OAD data, two methodologies, *SArA* and *GeneSys*, are applied in sequence. The *SArA* methodology focuses on the functional-logical definition of the OBS architecture, utilizing model-based systems engineering (MBSE) techniques [24]. This step establishes the functional structure of the system and its logical interdependencies. Furthermore, *SArA* enables rapid exploration of the solution space and identification of the most promising architectural solutions by means of a comprehensive requirements management, database-driven knowledge [30] and technology management [31], safety assessment [32], and early functional integration testing [33]. The promising, pre-selected OBS architecture is handed over to *GeneSys* for physics-based, parametric conceptual systems design.

In *GeneSys*, first, the system components are geometrically placed within the aircraft model and physically interconnected using representative elements such as ducts, pipes, or electrical cabling as specified by the functional-logical architecture model created in *SArA*. This step results in the generation of a detailed system topology as depicted in Figure 9 (Chapter 3.1). Second, preliminary component sizing is carried out based on physics-based and semi-empirical scaling laws derived from manufacturer data or detailed system design (DSD) methods. This step yields estimates for relevant key design parameters, such as component masses, total system masses, volumes, and

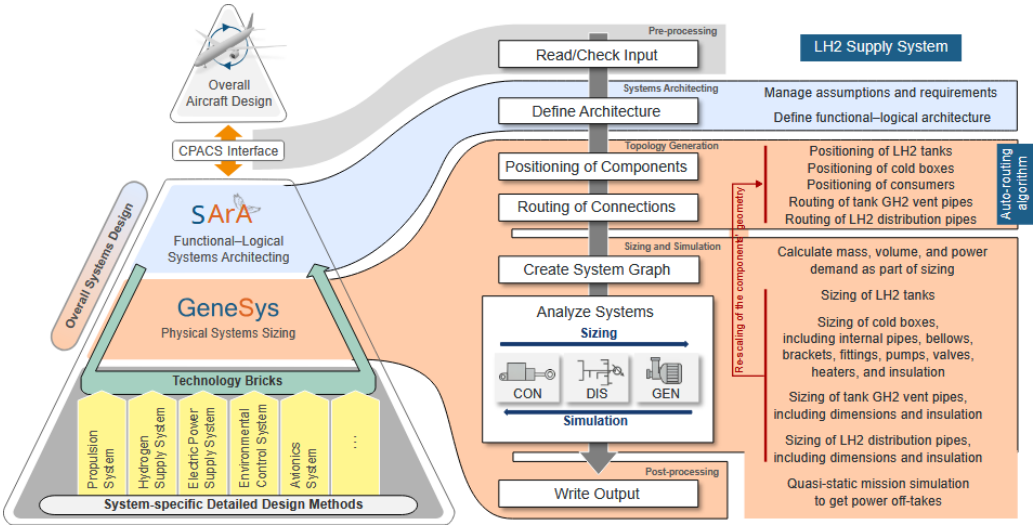


Figure 3 – Overall Systems Design framework with integrated LH_2 system conceptual design, adapted from [29]

CoG positions. As a final step, *GeneSys* performs a quasi-static simulation of the system's behaviour over a representative mission. This simulation provides estimates of the power demands placed on the propulsion system, specifically bleed air and shaft power requirements [20, 25, 26, 34, 35].
The conceptual sizing of the LH_2 supply system is integrated into the OSD framework. It supports the parametric conceptual design of a cryogenic LH_2 supply system for hydrogen powered aircraft. The objective of the sizing routine is to estimate mass, dimensions, thermal losses under defined operating conditions and component-level constraints. For the routing of the LH_2 pipes, an auto-routing algorithm is employed to consider allowable routing zones and segregation rules with regards to other OBS, e.g., the electric supply system [36]. A comprehensive breakdown of the LH_2 supply system sizing methods is provided in [37].

2.2.1 Geometric Layout of the LH_2 System Components

Figure 4 depicts the geometric layout of the two LH_2 tanks and the associated cold boxes as well as the assumed H_2 pipe cross-section. In general, the volume of each tank is calculated based on the storage pressure and the required LH_2 fuel mass, considering ullage and unusable fuel volume. The insulation thickness is determined based on the allowable heat ingress into the tank, which results from the defined dormancy time requirement using steady-state heat conduction. A more detailed analysis of the tank structure and its insulation is provided in [38]. For the cold box, a cylindrical container is assumed, housing the relevant components for tank pressure management and LH_2 distribution. The two cold boxes are arranged in a nested configuration to save space along the length of the fuselage. They may be arranged either one above the other or side by side. The required volume of the cold box is calculated, and the corresponding diameter and length are defined. With regard to hydrogen pipes, both the tank GH_2 venting pipe system and the LH_2 distribution pipe system are sized. According to Figure 4, it is defined that both the GH_2 and the LH_2 pipe consists

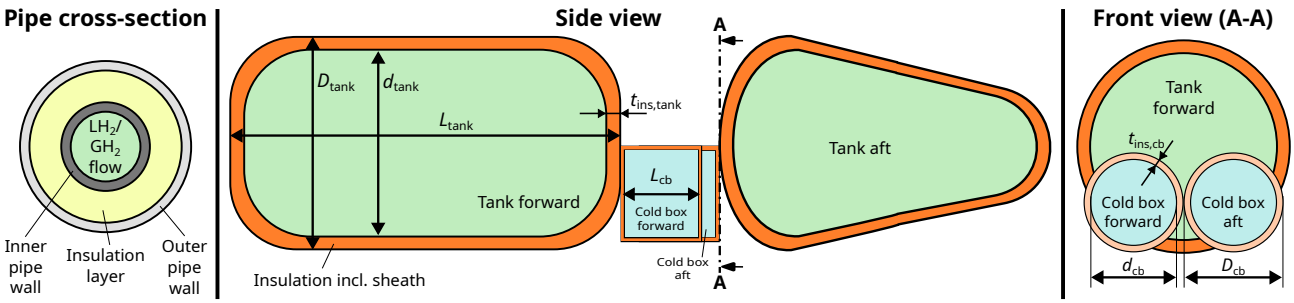


Figure 4 – Geometric layout of the tanks and cold boxes, and cross-section of the LH_2/GH_2 pipe

of an inner pipe, an insulation layer, and an outer pipe. The inner diameter of the inner pipe is calculated based on the occurring mass flow rates. The inner pipe wall thickness is sized by burst pressure. Subsequently, the insulation thickness and, thus, the inner diameter of the outer pipe are derived based on the insulation medium and the assumed maximum allowable heat ingress. Finally, the outer pipe's wall thickness is calculated based on the assumed pressure of the insulation medium. For solid insulation materials, a fixed wall thickness is assumed, since in this case, the outer pipe only represents a protective layer.

2.2.2 Parameter Assumptions for the LH_2 System Sizing

Table 2 summarizes the design assumptions for the LH_2 supply system. Tank parameters encompass operating pressures, LH_2 mass and volume constraints, as well as geometric and material properties.

Parameter	Unit	Value
LH_2 tanks		
Nominal pressure	bar	1.2
Venting pressure	bar	2.5
Burst pressure safety factor	-	1.5
Dormancy time	h	6
Ullage volume	%	3
Unusable LH_2 volume	%	7
Insulation material	-	Polyurethane foam
Wall material	-	2219 aluminium alloy
Cold boxes		
Insulation material	-	Aerogel
Insulation thickness	m	0.1
LH_2 and GH_2 pipes		
LH_2 max. mass flow rate per engine	kg/s	0.33
LH_2 max. flow velocity	m/s	9
GH_2 max. flow velocity	m/s	20
Distribution nominal pressure	bar	5
Burst pressure safety factor	-	1.5
Insulation material LH_2 pipe	-	Vacuum
Insulation material GH_2 pipe	-	Nitrogen
Wall material inner/outer pipe	-	Stainless steel
Max. heat ingress	W	20
Pipe thermal conductivity	W/(m · K)	16.3

Table 2 – Sizing parameter and assumptions for the LH_2 supply system design

Regarding volumetric constraints, Burschyk et al. [38] state that the tank's ullage volume can be assumed to be 3%. Furthermore, [39] defines the total unsuable fuel mass (comprising ullage and unpumpable LH_2) as 10%. Consequently, excluding the ullage volume, an unsusable LH_2 mass fraction of 7% is adopted. For the cold boxes, assumptions regarding the diameter and the insulation are required. The components inside the cold box are already insulated, but to further decrease heat ingress, each cold box comprises a layer with Aerogel insulation with a fixed thickness. This is a relevant aspect for the mass estimation of the cold boxes. A volume safety factor of two, accounting for a limited packing density of the components within the cold box housing, is applied. The sizing of the pipe system depends on the flow rates and velocities. Furthermore, assumptions are made regarding the pipe and insulation materials, as well as the allowable heat ingress. Using the assumed roughness, the pressure losses occurring from the distribution pumps to the cold boxes and then to

the engine can be determined. The LH_2 needs to be delivered to the engine perimeter at 5 bar. As part of the engine subsystem architecture, the LH_2 is conditioned and compressed to high pressures.

2.3 Hydrogen Direct-Combustion Engine

The conceptual engine design is developed using the virtual propulsion framework GTlab [40, 41, 42], while thermodynamic cycle analyses are performed with the DLR performance program (DLRp2) with an appropriate gas model for hydrogen [43]. Figure 5 presents the engine schematic that accounts for basic integration effects of the hydrogen conditioning system on engine performance: To preheat the hydrogen to 300 K at cruise conditions, the customer bleed, engine oil and core exhaust gas are used as heat source. The pressure losses and energy extraction of the recuperating heat exchanger (HEX) in the core exhaust section as well as the required power to drive the high-pressure hydrogen pump are fed back into the performance calculation.

The multidisciplinary engine design workflow employs a multi-point design strategy. Thrust, power, and bleed requirements are determined for take-off, end-of-field, second-segment, top-of-climb, and cruise conditions. Cycle parameters are then estimated to deliver the required thrust and off-takes across all operating points without violating technological limits. Based on the resulting cycle data, a knowledge-based method is used for flow-path sizing, and engine mass is derived using part-based semi-empirical correlations following [44] and applied in [45]. An initial estimate for the mass of the engine's hydrogen conditioning system is included. A simplified aerodynamic analysis uses the geometric flow-path definition in combination with cycle data to compute velocity triangles as well as mean flow and loading coefficients for all turbomachinery components. Component polytropic efficiencies are predicted using a correlation-based approach that accounts for entry-into-service effects, operational conditions, component loading, and size, as described in [46]. Spool speeds are constrained by turbine disk loading limits and by circumferential speed limits at compressor inlets and at the low-pressure turbine exit. These predicted efficiencies and spool speeds are iteratively propagated through all disciplinary models until convergence is achieved.

For the selected engine configuration, thrust ratings are defined and performance maps covering the operational envelope between minimum and maximum rated thrust are generated as functions of Mach number and altitude. These maps, together with the engine dimensions and mass, serve as inputs to the aircraft design process. Engine sizing is manually iterated until the available engine thrust and the required thrust of the overall aircraft configuration converge.

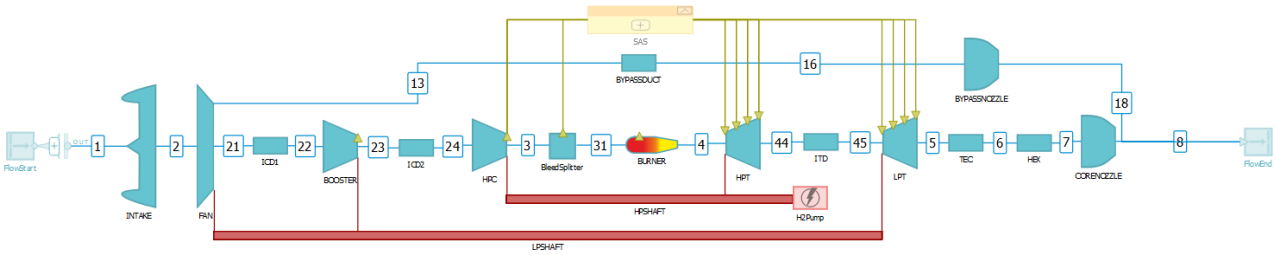


Figure 5 – Schematic LH_2 engine architecture for an unmixed geared turbofan engine with recuperative heat exchanger and an additional power-off take for the LH_2 high-pressure pump

2.4 Crashworthiness Demonstration

The integration of LH_2 tanks is a critical challenge in LH_2 aircraft design, as safety levels must align with conventional standards despite the current lack of defined crashworthiness certification requirements. This study addresses these uncertainties through full-scale simulations focusing on fuselage breakup, longitudinal crash loads, and local loads within the rear fuselage.

2.4.1 Crashworthiness Demonstration Strategy

The present study focuses on the development of a framework for analysing LH_2 tank integration concepts for the DLH25. The method covers the steps from model generation to concept evaluation across multiple scales, including the component, major component and full-scale levels. It is based on a crash demonstration strategy for LH_2 tank integration, which was developed as part of several

research projects at DLR [47], as illustrated in Figure 6. In addition to the framework development, the proposed approach is applied to a representative crashworthy LH_2 tank integration concept to evaluate the method. The analysis evaluates crash energy absorption, crash kinematics, as well as the response of tank mounts and acceleration levels in the rear fuselage section with integrated LH_2 tanks. Cabin safety aspects and potential crash effects of the novel rear fuselage on the cabin area are not considered.

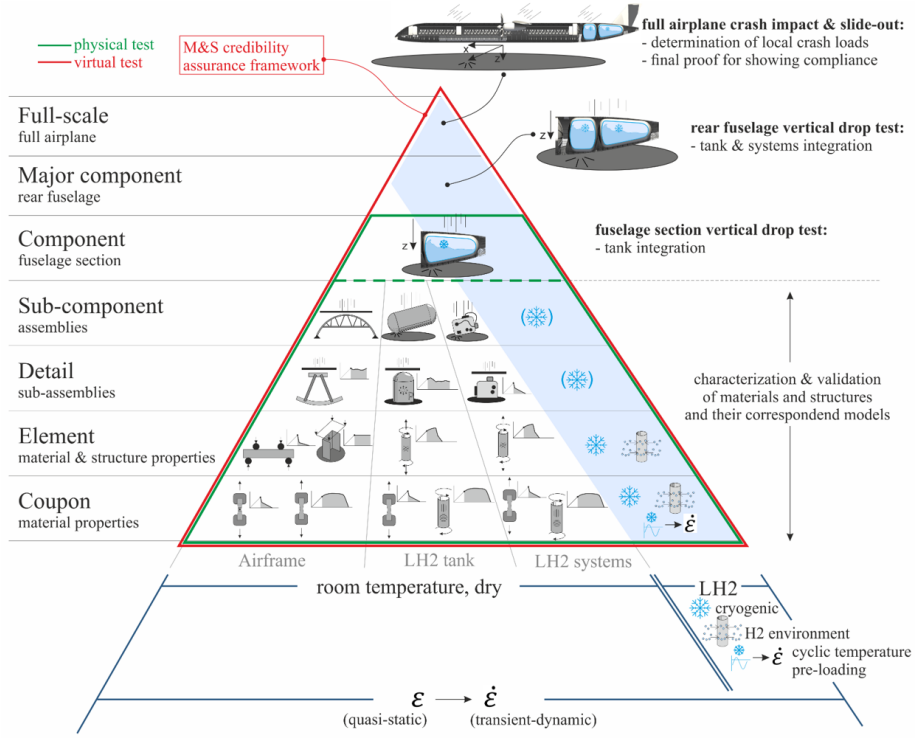


Figure 6 – Proposal of a crashworthiness demonstration strategy for LH_2 tank integration (adapted and redrawn from [47], licensed under CC BY 4.0)

Based on this approach, several finite element models for the DLH25 configuration were generated as shown in Figure 7. The simulation models are divided into three groups: Component level, Major component level, Full-scale level.

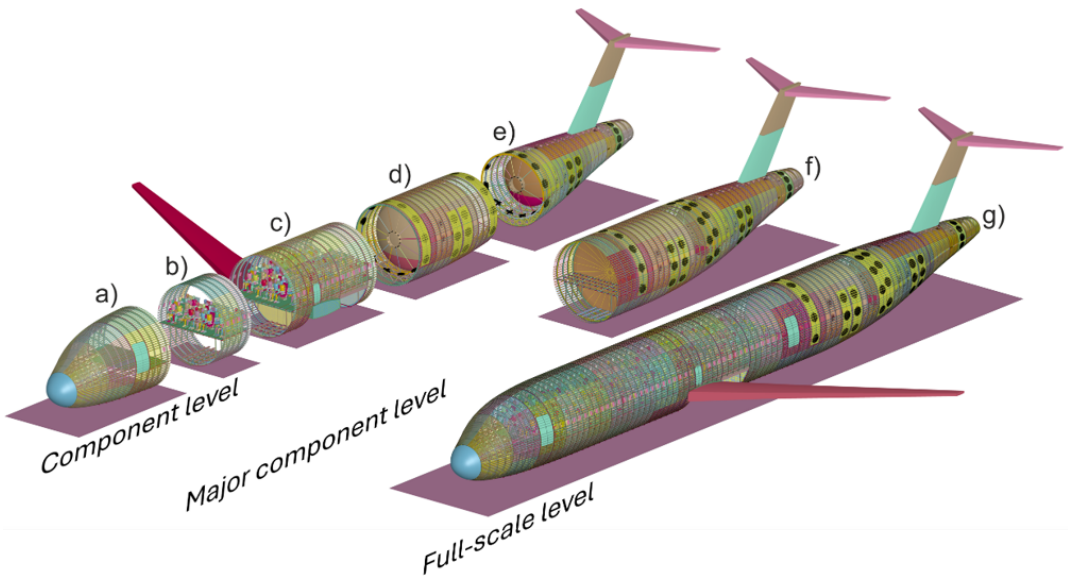


Figure 7 – Model overview

Before moving to the component, major component, and full-scale models, the fuselage section models of the cockpit (a) and cabin regions (b) and (c) are analysed to confirm the FE model response. At the component level, the fuselage section models with forward (d) and rear LH_2 tanks (e) are used to analyse the crashworthy tank integration concept including limiting tank accelerations, preventing tank intrusion and limiting tank deformation. At the major component level, the extended rear fuselage model containing both tanks (f) is used to investigate crash interactions of tanks, systems and the rear pressure bulkhead. At the full-scale level, the full airplane model (g) is used for both, the assessment of local crash loads at the tanks under real-world crash conditions, and for the final proof of the concept including a combination of horizontal and vertical impact conditions as well as airplane slide-out effects [47].

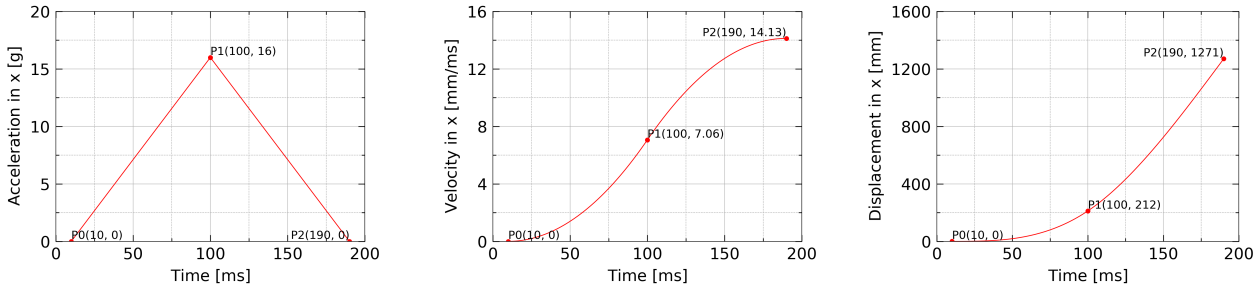
2.4.2 Crash Load Cases

Crashworthiness requirements and load cases for showing compliance with certification rules are not yet defined for LH_2 aircraft concepts. Based on today's certification specifications and published special conditions for other novel designs, crashworthiness requirements and load cases for LH_2 tank integration into transport airplane were derived by DLR [47]. These requirements and load cases solely represent a scientific view and shall support research work. These derived load cases consider three categories: (a) fuel tank integrity drop tests at the fuselage section level, (b) airplane level crash impact scenarios, and (c) airplane level sliding on the ground scenarios. In this section, load cases are discussed that are used to analyse the fuselage section and full airplane FE models.

Component and major component levels

1) Vertical drop test with v_z = 9.14 m/s (30 ft/s). This load case is based on FAA special conditions [48, 49] which are required for novel airplane designs, as well as various FAA/NASA drop test and full-scale airplane crash tests [50, 51].

2) Horizontal 16 g triangular acceleration pulse, as shown in Figure 8a, including corresponding velocity change (Figure 8b) and displacement change (Figure 8c). This load case is based on EASA CS 25.562 [52] (Emergency landing dynamic conditions), as well as FAA sled tests documented in [53, 54, 55, 56]. The requirements for this load case are higher compared to CS 25.561 mass retention requirement. The motivation for the 16 g pulse is that the LH_2 tank masses are located behind the cabin and breaking loose would result in catastrophic failure. Therefore, these masses should meet at least the same requirements as the seat and restraint systems which are related to in CS 25.562.



(a) Triangular acceleration pulse (b) Resulting velocity change (c) Resulting displacement change

Figure 8 – Triangular 16 g acceleration pulse for the horizontal load case and resulting kinematic response

Full-scale level

1) Purely vertical load case with v_z = 9.14 m/s (30 ft/s), v_x = 0 m/s, pitch angle 0° and friction coefficient of 0.3 between the impact surface and the fuselage. This load case is analysed to evaluate the influence of higher full fuselage mass compared to the fuselage section drop tests. This load case is based on [57].

2) Combined load case with v_z = 9.14 m/s (30 ft/s), v_x = 80 m/s (262 ft/s), pitch angle 0° and friction coefficient 0.8 between the impact surface and the fuselage. By increasing the friction coefficient, this load case simulates a crash landing on soft soil without explicitly modelling the soil. It is analysed to evaluate the influence of combined vertical/horizontal impact velocity and high friction coefficient on the tank mounts loads at the full-scale level that are compared with the horizontal load case on the fuselage section level. This load case is based on [57].

3. Component Design Studies

The primary objective of this chapter is to advance the design maturity of the DLH25 by transitioning from technical assumptions to technical specifications for certain disciplines. Specifically, the on-board and LH_2 system architectures are derived based on the initial aircraft concept. The resulting specifications for power and bleed air offtakes, in conjunction with the thrust requirements derived from the conceptual design, serve as essential boundary conditions for the subsequent development of the LH_2 UHBR engine. Finally, the chapter describes the initial crash concept, followed by an analysis of the structural integration of the LH_2 tanks through crash simulations.

3.1 On-Board Systems Architecture

The following chapter presents the integration aspects and conceptual sizing results of the DLH25's overall on-board systems architecture. The emphasis is placed on the on-board LH_2 supply system, and a comparison is made with the corresponding on-board system architecture of a technologically equivalent SAF research baseline. The OBS topology of the DLH25 as an output of the OSD framework is depicted in Figure 9. It comprises all major mass and power relevant OBS and is generated based on the aircraft geometry using knowledge-based and auto-routing algorithms [36].

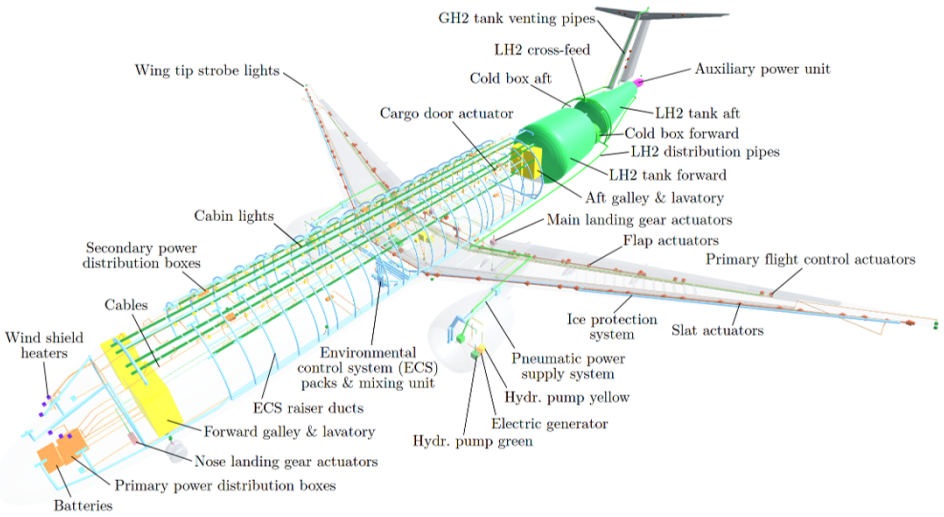


Figure 9 – Topology of the on-board systems of the DLH25 as an output from the OSD framework

3.1.1 Definition of the On-Board LH_2 Supply System Architecture

Figure 10 shows the functional-logical representation of the defined reference architecture of the LH_2 system of the DLH25. The main subsystems comprise two LH_2 tanks, two cold boxes with one cold box for each LH_2 tank, a GH_2 venting pipe system and a LH_2 distribution pipe system.
The cold box houses all components required for the pressure and temperature management of the tank, overpressure safety functionalities, and the LH_2 distribution pumps in an integrated unit. The components inside the cold box themselves are insulated, and additionally, the cold box housing features an insulation layer for minimum heat ingress. A fraction of the LH_2 mass flow from the tank is vaporized by means of electric heaters to maintain the pressure inside the tank as soon as the fuel level decreases. Both, the LH_2 distribution pumps and the electric heaters are installed in a parallel-redundant configuration.

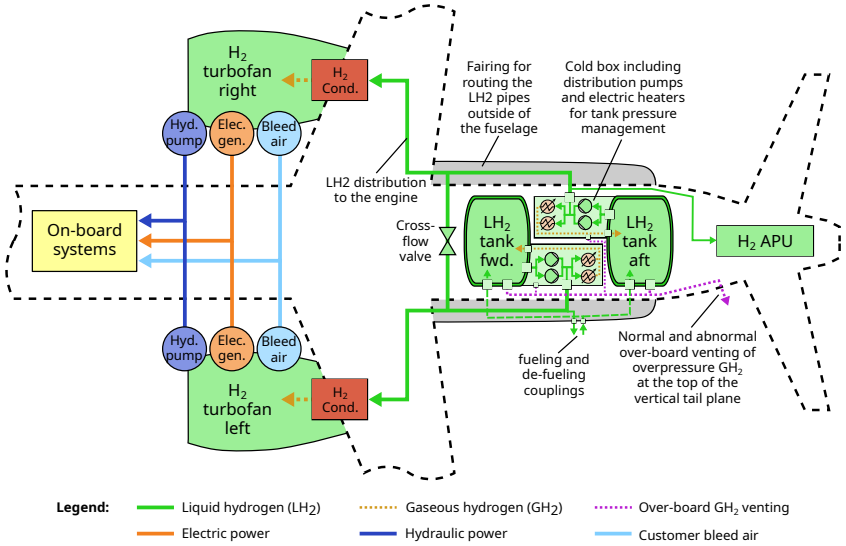
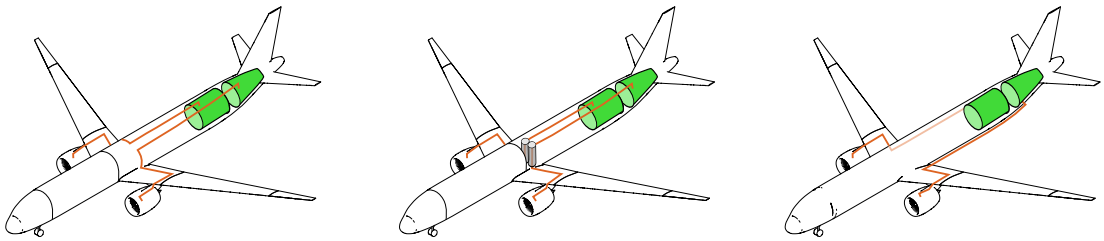


Figure 10 – Schematic LH_2 on-board system architecture of the DLH25

Moreover, both tanks comprise a normal venting system to release overpressure GH_2 and an abnormal venting system, which prevents tank bursting in case the normal venting system malfunctions. For safety reasons, the cold box features an abnormal venting system as well in case of abnormal pressure build-up inside the cold box. The tanks can be fueled and defueled via the ground connectors. Both tanks are connected to a single fueling and a single defueling connector. The flow of hydrogen is controlled via dedicated flow valves.
During normal operation, each tank supplies one engine. For abnormal operation or if the tanks have different fill volumes, a cross-flow valve connects each tank with every engine. The auxiliary power unit (APU) comprises an H_2-powered gas turbine and is nominally supplied by the aft LH_2 tank. The LH_2 is transported to the engines via the pipe network. As outlined in Section section 3.2, the liquid hydrogen is subjected to a conditioning process using engine heat prior to combustion within the engine.

3.1.2 GH_2/LH_2 Pipe Routing Concepts

The routing of the tank venting pipes follows a direct path and does not necessitate a more sophisticated analysis. The GH2 venting pipes are routed from the tanks along the leading edge of the vertical stabilizer, with the GH2 outlet situated at the top of the vertical stabilizer. However, for the LH_2 pipe routing between the LH_2 tank and engine perimeter, different concepts, as depicted in Figure 11, are analysed. The LH_2 pipe routing concept poses a particular challenge for low-wing configurations such as the DLH25, as the pipes eventually interfere with the cabin or the emergency exits, whilst at the same time they must not significantly affect either the primary airframe structure or the aerodynamic characteristics of the aircraft. The LH_2 pipes must not be routed within the pressurized cabin area, since in case of leakages, the passengers are directly exposed to a potential flammable gas. In the wing area, the pipes should be routed through or along the spars wherever possible. With respect to the development of relevant LH_2 pipe routing concepts, the three approaches depicted in Figure 11 are discussed in the following.
The upper routing options, whether placed externally (Figure 11a), between fuselage frames (Figure 11a), or via non-pressurized channels (Figure 11b), either degrade aerodynamic performance through necessary fairings or require significant structural reinforcements. In contrast, the lower routing (Figure 11c) along the rear fuselage minimizes aerodynamic drag and structural mass by avoiding both cabin penetration and fairings. Despite its proximity to the rear emergency exit, the lower routing is selected for its lower system complexity and minimal aerodynamic impact. The resulting safety risk at the rear emergency exit is addressed by segmenting the LH_2 pipeline with shut-off valves, allowing for rapid flow interruption in case of an emergency.
Ongoing design considerations include LH_2 return lines to decouple supply and consumption dynamics and manage transient fluctuations. A trade-off analysis between a liquid recirculation loop and



(a) Upper routing (b) Upper routing through cabin (c) Lower routing

Figure 11 – Different LH_2 pipe routing concepts for the DLH25

a buffer tank in the wing's non-cryogenic section, as well as evaluations of GH_2 recirculation and wingtip venting for hydrogen dispersion, are beyond the scope of this study and require separate analysis.

3.1.3 LH_2 Supply System Conceptual Design Results

A key aspect in the scope of applying the OSD framework for overall OBS design is the design of the on-board LH_2 supply system. Table 9 (Appendix) lists the results of the relevant system components concerning geometry, mass, and power demand. For cost-efficiency and ease of industrialization, a standardized cold box unit is used, resulting in both units being identical. The distribution system comprises two separate networks: LH_2 pipes routed from the tanks to the engines, and GH_2 venting pipes routed to the tip of the vertical stabilizer.

3.1.4 Overall System Mass Results

Figure 12 illustrates the mass delta of the DLH25 by comparing it to the SAF-powered DLR-F25. Most conventional systems exhibit negligible mass deviation, which is attributable to the comparable on-board systems architecture. The mass of the ice protection system is reduced for the DLH25 due to geometric modifications. Despite the system's low baseline mass, these changes result in a significant impact. Variations in landing gear actuation, lighting, APU, and utility systems (hydraulic and pneumatic) result from geometrical differences between the DLR-F25 and DLH25, such as varying cable and pipe lengths. Particularly for the hydraulic power supply system, the increased fuselage length and the T-tail configuration of the DLH25 (Figure 27) compared to the DLR-F25 necessitate a greater pipe routing length. Consequently, this results in a higher hydraulic fluid volume and additional pipe brackets, leading to an increase in system mass. The LH_2 supply system constitutes 44% of the DLH25's total system mass. Compared to the DLR-F25 fuel system, this represents a mass increase of 1490%, underscoring the significant challenges associated with the mass integration of hydrogen infrastructure. The integration of the LH_2 supply system also impacts the electrical power system, which increases in mass by 13% due to the higher power demand required for LH_2 distribution pumps and electric heaters for tank pressure management. The LH_2 conditioning system is excluded from this analysis, as it is attributed to the engine. Across all systems, the overall mass delta between the DLR-F25 and the DLH25 is 75%. Figure 13 compares the on-board and LH_2 storage and system masses with the previous iteration of the DLH25 [19]. The total delta across all on-board system masses excluding LH_2 related masses is 4.9%, resulting from the transition of OEM-based sizing in the previous design to a physics-based approach considering actual system locations within the aircraft. Further changes are observed within the LH_2 storage and systems masses. Specifically, the total structural mass of both LH_2 tanks decreases from 5630 kg to 5170 kg. This reduction is attributed to an improved gravimetric index (GI), due to an optimized volume distribution, a reduction in the unusable fuel mass fraction, and a lower total fuel requirement due to the increased efficiency of the DLH25 (see Chapter 4.). Conversely, the LH_2 system architecture shows a mass increase of 510 kg, primarily attributable to the detailed routing of the piping system. These effects nearly offset one another, such that the net reduction of 3.4% in total LH_2 storage and systems mass is mainly a result of the decreased unusable fuel mass.

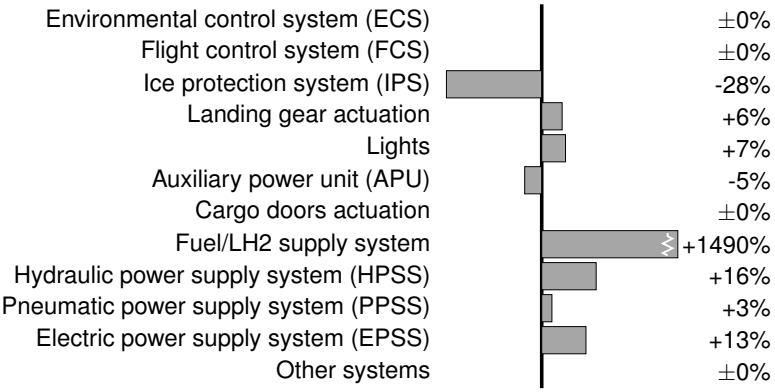
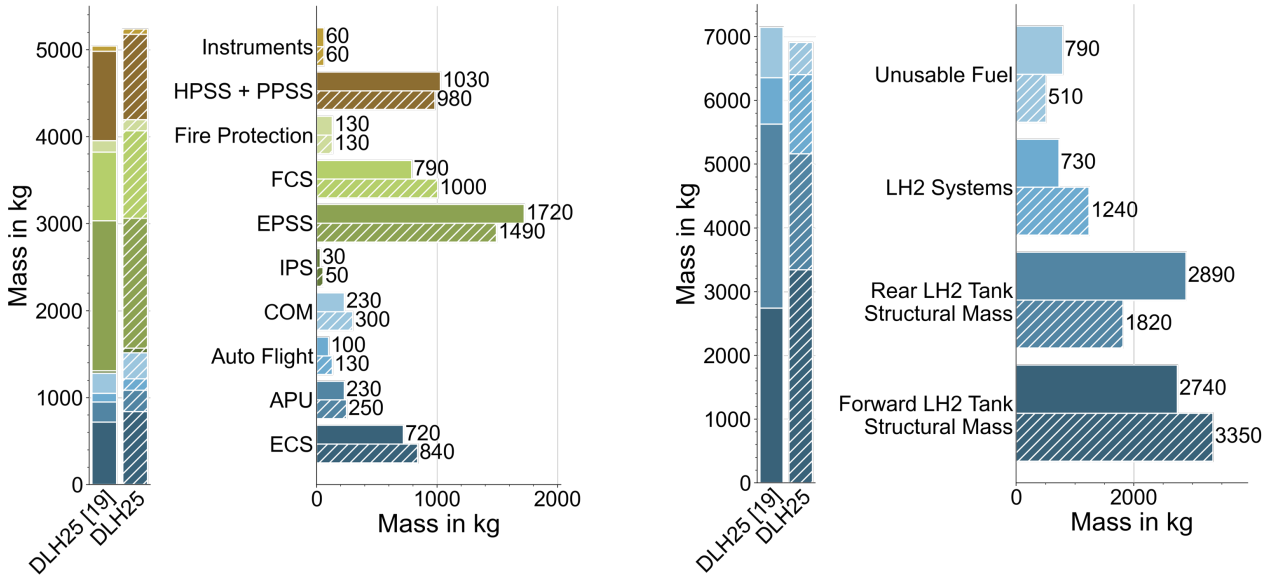


Figure 12 – Changes in the on-board systems masses of the DLH25 compared to the DLR-F25



(a) On-board systems (excl. LH_2 systems)

(b) LH_2 storage and systems

Figure 13 – On-board system and LH_2 systems mass breakdown comparisons for the initial DLH25 [19] (solid) and the updated DLH25 (hatched)

3.1.5 Engine Power Off-Take Results

This section summarizes the engine bleed air and power off-takes required by the OBS for the design mission of 2500 nautical miles. First, Figure 14 depicts the customer bleed air demands per engine, comparing the SAF-powered DLR-F25 with the DLH25. The bleed air mass flow peaks during climb and descent are characterized by the engagement of the ice protection system. The continuous mass flow during cruise contributes to the environmental control system. Since the passenger amount for both aircraft, the DLR-F25 and the DLH25, is equal, the demand of the environmental control system is similar. The small differences between the two aircraft originate from the different mission profiles and the slightly different wing geometry, and thus different ice protection sections at the wings.
In Figure 15, the mechanical engine shaft power off-takes per engine are illustrated. Specifically, the total demands are characterized by the sum of all individual on-board hydraulic and electric consumer demands. Smaller peaks are visible at the beginning and towards the end of the mission profile that can be attributed to the operation of the landing gear and high-lift systems. Otherwise, the base load shown represents the operation of a large number of electrical loads as well as the total internal hydraulic leakage. The shaft power peaks mid-cruise originate from the operation of the galleys. In general, the shaft power demand is higher for the DLH25 (61 kW) than for the DLR-F25 (50 kW), due to the higher LH_2 distribution pump power compared to kerosene pumps and the required electrical power for LH_2 vaporization for the tank pressure management.

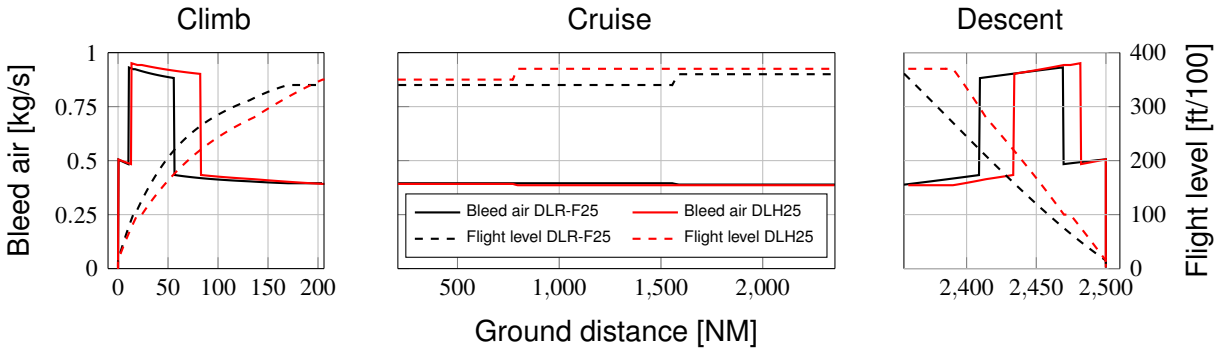


Figure 14 – Mission bleed air demand of the DLH25 in comparison to the DLR-F25 for one engine

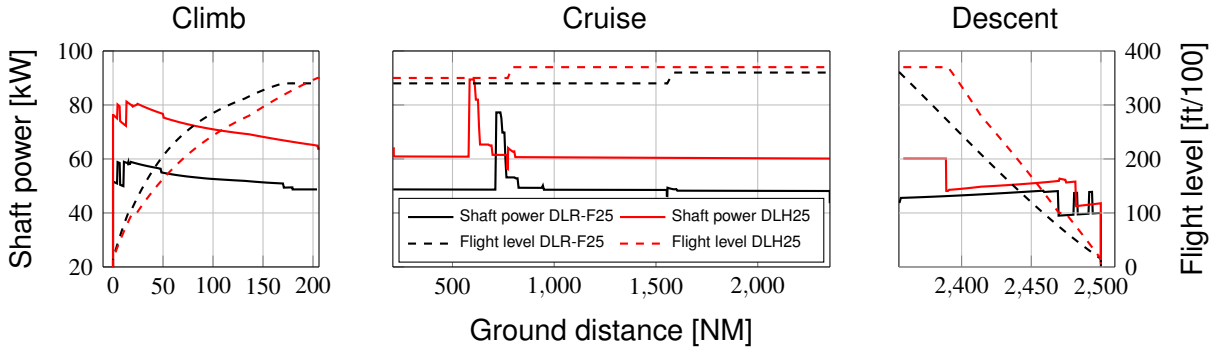


Figure 15 – Mission shaft power demand of the DLH25 in comparison to the DLR-F25 for one engine

3.2 Hydrogen Direct-Combustion Engine

This section presents the characteristics of the hydrogen direct-combustion engine of the DLH25 in direct comparison to the the DLR-F25 baseline engine operated with kerosene or SAF. Engine requirements are provided in Table 3 and performance characteristics are shown in Table 4. Required heat flows for hydrogen pre-conditioning are depicted in Figure 16 and engine flow path dimensions are shown in Figure 17.

3.2.1 Engine Requirements Results

The sizing engine conditions for the configurations DLR-F25 and DLH25 do not differ in altitude and Mach number requirements. While also customer off-takes are the same, the DLH25 requires more power off-takes to supply aircraft on-board systems (Chapter 3.1.5). Table 3 presents data for the operating conditions mid cruise of the typical misson, Top-of-Climb (TOC) as a hypothetical maximum sizing condition to ensure optimal step climbs and Maximum Take-Off (MTO) both at a standard and hot day for the design misson as well as End-of-Field (EOF) and 2nd Segment (2ndSeg) for one engine inoperative. The thrust demand of the DLH25 aircraft is significantly higher compared to the DLR-F25 baseline aircraft (see Table 3). The required thrust is 28 % increased at mid cruise of the typical mission and 16 % for the sizing maximum top-of-climb (TOC) condition.

3.2.2 Engine Performance Results

The engine performance results are presented in Table 4. The fuel heating value of hydrogen is with 119.1 MJ/kg significantly higher compared to Jet-A1 with 43.3 MJ/kg. Therefore, the fuel-to-air ratio is $\approx$ 60 % lower for the hydrogen engine. The combustion of hydrogen produces much more water compared to kerosene. Due to the high amount of water, the exhaust gas that enters the turbines has $\approx$ 6 % higher specific heat capacity and thereby, allows to extract more specific turbine work compared to the kerosene case. The high heat capacity increases the fuel efficiency of the

Parameter	Unit	Configuration	Cruise	TOC	MTO-0	MTO-15	EOF	2ndSeg
Thrust	[N]	DLR-F25	17828	23046	124710	124710	86872	76109
		DLH25	22847	26760	143990	143990	103300	82590
		rel. Dev. %	28.2	16.1	15.5	15.5	18.9	8.5
Thrust	[lbf]	DLR-F25	4008	5181	28036	28036	19530	17110
		DLH25	5136	6016	32370	32370	23223	18567
Mach number	[-]	DLR-F25	0.78	0.76	0	0	0.228	0.239
		DLH25	0.78	0.76	0	0	0.239	0.250
Altitude	[m]	DLR-F25	11277.6	11277.6	0	0	11	122
		DLH25	11277.6	11277.6	0	0	11	122
Flight Level	[100ft]	DLR-F25	370	370	0	0	0	4
		DLH25	370	370	0	0	0	4
ΔT_{ISA}	[K]	DLR-F25	0	10	0	15	15	15
		DLH25	0	10	0	15	15	15
Power Off-Take	[W]	DLR-F25	-50	-50	-95	-95	-95	-95
		DLH25	-60	-60	-140	-140	-140	-140
		rel. Dev. %	20.0	20.0	47.4	47.4	47.4	47.4
Custombler Bleed	[kg/s]	DLR-F25	0.425	0.425	0	0	0	0
		DLH25	0.425	0.425	0	0	0	0

Table 3 – Overview of engine requirements and direct comparison between DLR-F25 and DLH25 for different operating conditions: Cruise, Top-of-Climb (TOC), Maximum Take-Off (MTO), End-of-Field (EOF) and 2nd Segment (2ndSeg).

core engine and allows to reduce core size, i.e. an engine core operated with hydrogen is smaller compared to a kerosene reference providing the same output power.
The thrust ratio referring cruise to TOC increases from 0.77 to 0.85 for the LH_2 aircraft. The higher thrust ratio causes a higher power setting with increased temperatures and pressures at cruise conditions. Both engines are sized for T_{41} = 1707 K at maximum TOC and $T_{3,max}$ = 913 K at MTO. Due to the different thrust ratios, the operating temperature T_{41} is 49 K hotter, the overall pressure ratio (OPR) is 4 % and T_3 is 11 K higher at cruise operation for the DLH25 engine. A higher temperature T_{41} at cruise imposes challenges for service life and time on wing. An increased combustor inlet temperature T_3 increases the formation of NOx emissions. Furthermore, the fan face axial inflow Mach number is 2.7 % higher for the DLH25, since both engines are sized for the same flow capacity of the fan at TOC.
The bypass ratio (BPR) was optimized for the DLR-F25 engine as described in [20]. It is expected that the optimum BPR is in the same region for the DLH25 as for the DLR-F25 and therefore, BPR is set to 15.1 for both engines. This facilitates the comparison of both engines but eventually neglects a small potential for further optimization, which should be exploited in the future.
The change of the exhaust gas composition due to a higher amount of water for hydrogen direct-combustion does also affect the fan pressure ratio. The exhaust gas has more energy remaining after the expansion in the turbines and the core nozzle produces higher jet velocities. In order to maintain the optimal ratio of ideal nozzle velocities between the bypass and core nozzle (velocity ratio is equal to the transmission efficiency), also the ideal jet velocity of the bypass nozzle increases which requires a higher fan pressure ratio of 1.42 at cruise compared to 1.36 for the kerosene engine. The fan inlet mass flow increases with 10.3 % at TOC, which is less compared to the change in required thrust. This is caused by the higher ideal jet velocities and the higher specific power of the hydrogen-operated core engine. In combination with the increased fan pressure ratio, the corrected mass flow at the core engine's inlet indicates engine core size and is only 2.3 % higher at TOC even if the engine provides 16.1 % more thrust.
In total, the thrust specific energy consumption (TSEC) is 3.3 % lower at cruise for the hydrogen engine (DLH25) compared to the kerosene variant (DLR-F25). The more efficient use of chemical energy of hydrogen is mainly related to the higher specific heat capacity of the exhaust gas due to

more water resulting as the product of combustion and allowing to extract more specific energy from the exhaust flow.

Parameter	Unit	Configuration	Cruise	TOC	MTO-0	MTO-15	EOF	2ndSeg
TSEC	[J/s/N]	DLR-F25	620.0	626.6	270.3	279.0	386.6	391.6
		DLH25	599.2	610.8	277.9	287.7	399.4	402.5
		rel. Dev. %	-3.3	-2.5	2.8	3.1	3.3	2.8
OPR	[-]	DLR-F25	41.1	49.9	38.0	38.0	35.9	33.0
		DLH25	42.7	47.9	37.8	37.7	36.4	31.2
		rel. Dev. %	4.0	-3.9	-0.6	-0.8	1.4	-5.5
BPR	[-]	DLR-F25	15.1	13.6	14.2	14.2	14.9	15.4
		DLH25	15.1	14.2	14.7	14.7	15.3	16.2
		rel. Dev. %	0.0	4.8	3.1	3.0	2.3	5.1
Fan Pressure Ratio	[-]	DLR-F25	1.36	1.44	1.34	1.34	1.32	1.29
		DLH25	1.42	1.48	1.37	1.37	1.35	1.29
		rel. Dev. %	4.7	3.1	2.2	2.2	2.8	0.6
Fan Face ax. Mach	[-]	DLR-F25	0.620	0.684	0.503	0.503	0.502	0.476
		DLH25	0.637	0.682	0.511	0.511	0.518	0.468
		rel. Dev. %	2.7	-0.2	1.5	1.5	3.2	-1.8
Fan Inlet Mass Flow	[kg/s]	DLR-F25	224.3	227.2	563.2	549.0	564.5	538.6
		DLH25	251.4	250.6	627.9	612.1	638.4	588.0
		rel. Dev. %	12.1	10.3	11.5	11.5	13.1	9.2
FAR	[-]	DLR-F25	0.02556	0.02975	0.02834	0.03002	0.02946	0.02819
		DLH25	0.01031	0.01166	0.01137	0.01207	0.01197	0.01105
T3	[K]	DLR-F25	769	850	872	913	906	885
		DLH25	780	839	873	913	912	875
		rel. Dev. %	1.4	-1.3	0.1	0.0	0.7	-1.1
T4	[K]	DLR-F25	1632	1821	1799	1881	1859	1805
		DLH25	1680	1817	1824	1900	1894	1804
		rel. Dev. %	3.0	-0.2	1.4	1.0	1.9	0.0
T41	[K]	DLR-F25	1529	1707	1690	1767	1747	1696
		DLH25	1578	1707	1717	1790	1784	1699
		rel. Dev. %	3.2	0.0	1.6	1.3	2.1	0.2

Table 4 – Overview of engine performance characteristics and direct comparison between DLR-F25 and DLH25 for different operating conditions: Cruise, Top-of-Climb (TOC), Maximum Take-Off (MTO), End-of-Field (EOF) and 2nd Segment (2ndSeg).

3.2.3 Pre-Conditioning Heat Flow Results

The LH_2 high-pressure pump supplies the pre-conditioning system with pressurized fuel and requires an additional power off-take from the high-pressure shaft of 165 kW at cruise. The pre-conditioning system itself is not modelled here but it is expected that such a system is capable of providing enough heat to reach the targeted fuel temperature of 300 K for all operating points. Details on pre-conditioning system studies can be found in [43]. The required energy to preheat the pressurized hydrogen comes from different sources. The engine oil and the customer bleed dedicated for the aircraft's ECS are cooled. The remaining energy is recuperated from the engine exhaust flow using a heat exchanger after the turbine exhaust casing and upstream of the core nozzle. The recuperative heat exchanger is assumed to cause an additional pressure loss of 3 % during cruise operation. The resulting heat flows are presented in Figure 16. A total heat flow of up to 1317 kW is required at take-off and 435 kW at cruise. The heat flow during cruise operation is mainly provided by recuperation (50 %) and the oil system (35 %) while the share of cooling the customer bleed is rather low (15 %).

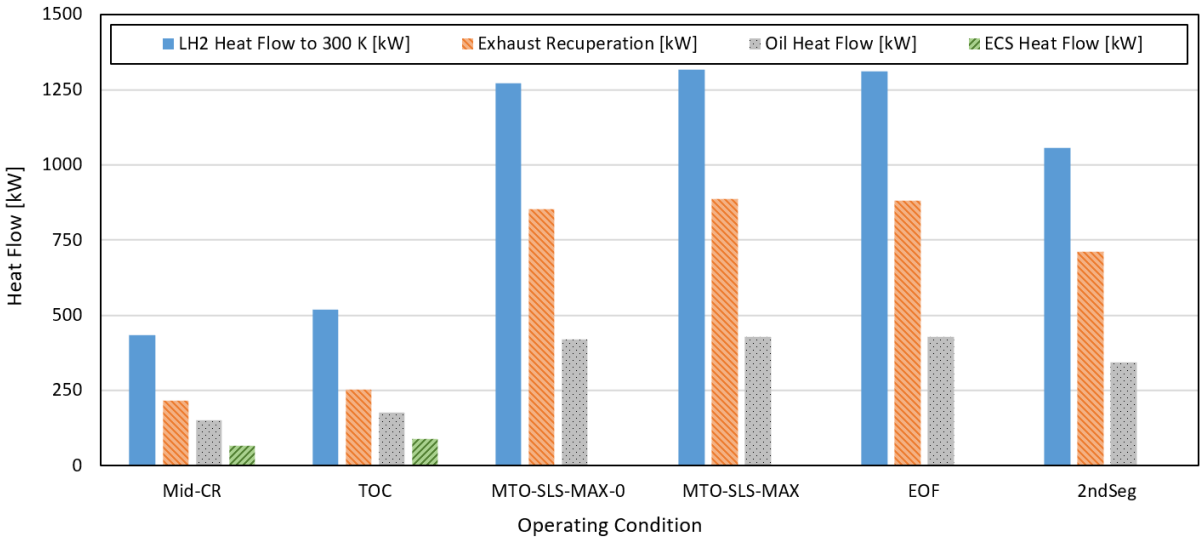


Figure 16 – Overview of required heat flows for LH_2 pre-conditioning to reach a fuel temperature of 300 K at relevant operating conditions

3.2.4 Engine Flow Path and Mass Results

Figure 17 shows the estimated flow path model of the DLH25 engine compared to the DLR-F25 SAF baseline engine. The fan diameter of the hydrogen engine is only 5 % larger while providing 16.1 % more thrust capability at TOC. The nacelle length increases by 2.5 % and its wetted area by 2.1 m^2. The total engine length increases by $\approx$ 0.4 m mainly due to the integration of the recuperative heat exchanger upstream of the core nozzle. The bare engine mass of the DLH25 is with 2814 kg heavier compared to the DLR-F25 engine ($\approx$ 8 %). It includes a rather optimistic mass allocation for the LH_2 pre-conditioning system resulting in +290 kg additional mass compared to a kerosene-based fuel and thermal management system.

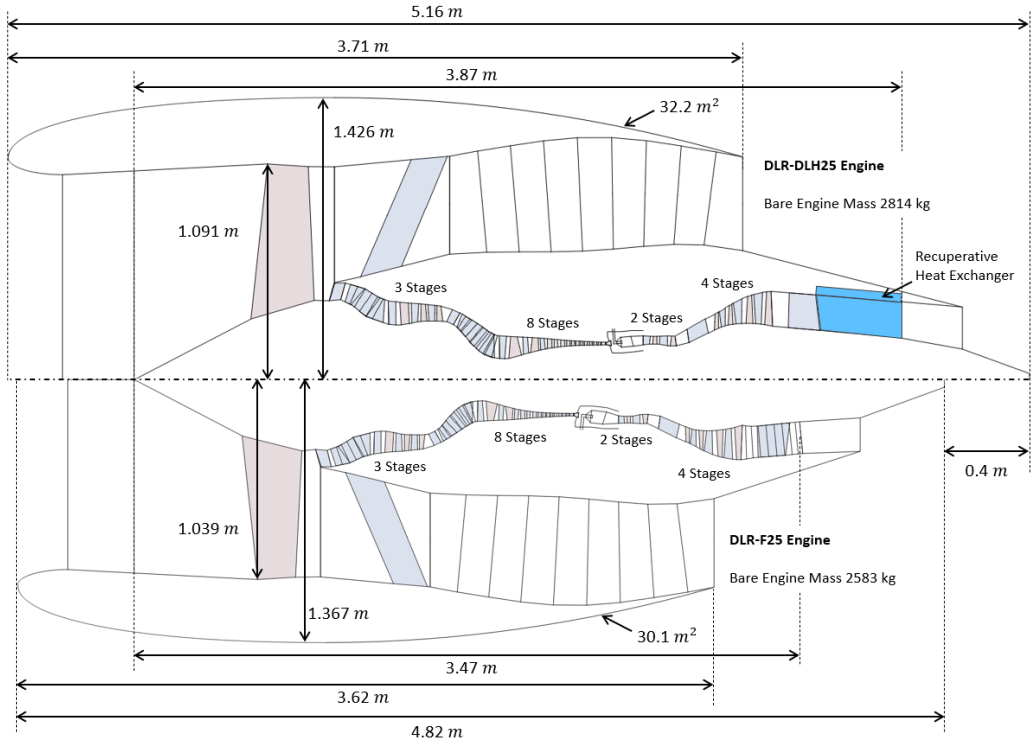


Figure 17 – Comparison of engine flow path models for the hydrogen direct-combustion configuration (DLH25) compared to the SAF baseline (DLR-F25).

3.3 Evaluation of Crashworthiness Demonstration Strategy

The crashworthiness demonstration strategy presented in Section 2.4 is utilized in the present section to evaluate the initial crashworthy LH_2 tank integration concept. The modelling of the fuselage, LH_2 tanks and the contained LH_2, as well as the tank integration concept are presented, followed by a discussion of the simulation results at component, major component and full-scale level.

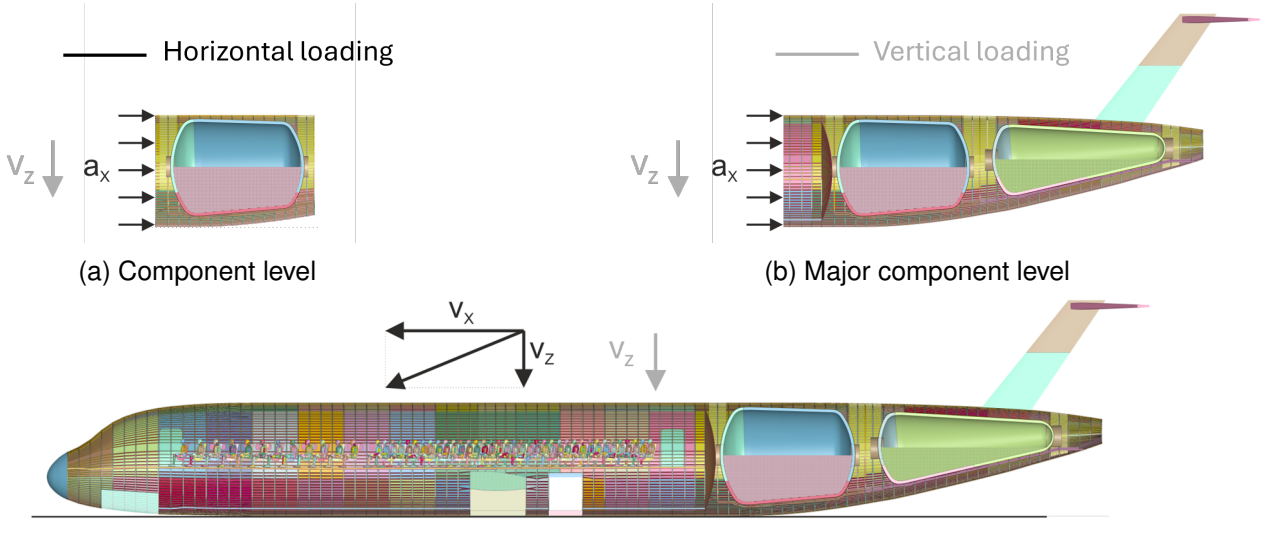
3.3.1 Setup of Crash Model

The structural modelling of fuselage sections and full-scale aircraft is carried out with DLR's process chain tool *Parametric Numerical Design and Optimization Routines for Aircraft (PANDORA)* [58]. This process chain tool enables the generation of models with varying level of detail depending on the application case [59]. The fuselage is modelled using a conventional stringer-frame design with typical aluminium alloys 2024 and 7075.

The LH_2 tank model for the crash simulations includes an inner shell (inner vessel) and an outer shell (outer jacket). In this simplified approach, the two shells are connected at the dome areas by continuous rings as shown for the forward LH_2 tank in Figure 19a. The inner vessel contains LH_2, while the outer jacket encloses the insulation layer. As part of the crash concept, the insulation layer between the two shells, with a thickness of 145 mm, was discretized using solid elements and the mechanical properties of aerogel were assigned [60]. This constitutes a conservative approach due to low stiffness and energy absorption capabilities of aerogel materials.

The liquid hydrogen was modelled using Smoothed Particle Hydrodynamics (SPH) according to [61], [62]. This approach aims to capture the dynamic fluid behaviour under realistic crash conditions and to estimate resulting sloshing loads on the LH_2 tank structure and its mounting system. Compared to conventional jet fuels (ρ_{JF} = 0.775 - 0.840 g/cm^3), LH_2 exhibits a substantially lower density of ρ_{LH_2} = 0.071 g/cm^3. Consequently, the sloshing effects of LH_2 are expected to be substantially lower compared to those of jet fuels. The SPH particles were generated using *LS-PrePost* 4.9.12. A constant particle spacing (pitch) of 35 mm was defined in x-, y-, and z-directions. As a generic example in this study, a liquid height corresponding to mid-height on the forward side of each tank was introduced to define a representative fill level. Due to the non-symmetric, conical geometry, this definition results in different volume fractions, corresponding to fill levels of 48.9% (forward tank) and 39.8% (rear tank). At these fill levels, the forward LH_2 tank contains 0.65 · 10^6 particles and the rear tank contains 0.23 · 10^6 particles.

The finite element (FE) models used for the crash simulations at the component, major component, and full-scale levels are shown in Figure 18. The load cases described in Chapter 2.4.2 are applied, with a distinction made between vertical (grey) and horizontally dominant (black) load cases during the evaluation of the results.



(a) Component level

(b) Major component level

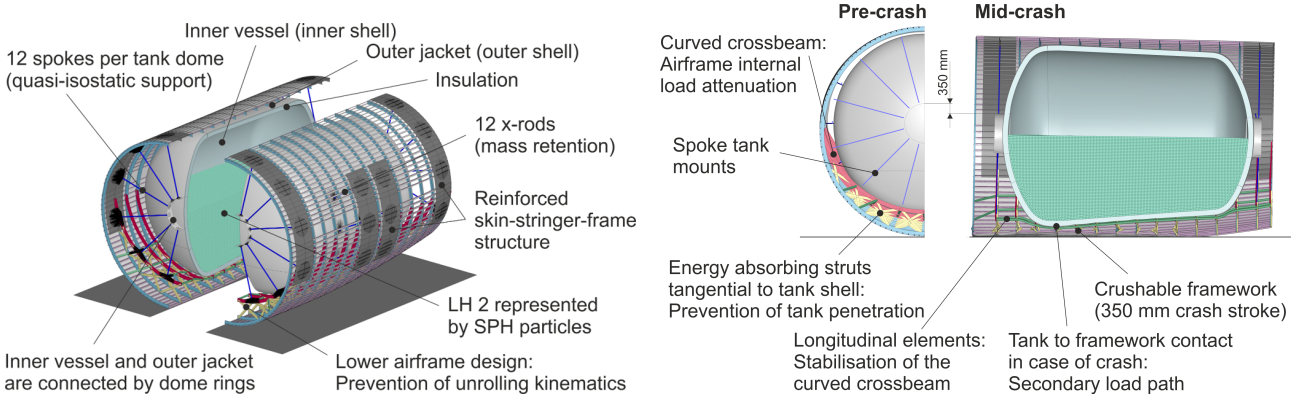
(c) Full-scale level

Figure 18 – FE models and the according vertical (grey) and horizontal (black) crash load cases

3.3.2 Initial Crashworthy LH_2 Tank Integration Concept

Design considerations for crashworthy LH_2 tank integration are discussed in [47]. The present study builds upon these findings. The crashworthy sub-structure is implemented as an energy-absorbing framework positioned beneath the LH_2 tank, as illustrated in Figure 19a and Figure 19b. It consists of a curved crossbeam that aligns with the LH_2 tank, the longitudinal elements and energy absorbing struts. The crushing distance of the struts is s = 350 mm. The wall thickness of the curved crossbeam is adjusted so that it can withstand the crushing loads from the energy absorbing struts and provide sufficient stiffness to prevent extensive compliance movement towards the LH_2 tank. The wall thickness of the energy absorbing struts is adjusted so that the crushing distance is maximized at an impact speed of 9.14 m/s (30 ft/s) at the fuselage section level. The longitudinal elements are intended to stabilize the curved crossbeam and the energy absorbing struts, and to prevent them from tilting under vertical loads.

This specific structural crash tank integration concept presented here was initially investigated as part of the Clean Aviation project FASTER H2 [63], [64]. As illustrated in Figure 19a and Figure 19b, the LH_2 tank is integrated into the fuselage via spokes and x-rods. The spokes extend from the tank dome to the fuselage, providing primary vertical support for the tank. In the lower fuselage region, specifically within the sub-tank framework, the spokes are connected to both the longitudinal elements and the curved crossbeam. A total of 24 spokes are employed to support the LH_2 tank, comprising 12 at the forward dome and 12 at the rear dome. Longitudinal support is provided by 12 x-rods that extend from the outer jacket to the fuselage, arranged in two parallel rows of six rods each. As illustrated in Figure 19a, the wall thickness of the fuselage patches (skin, stringers, and frames) surrounding the constrained interpolation nodes is conservatively increased to 8 mm.



(a) LH_2 tank integration concept

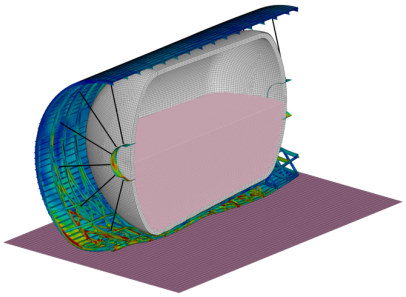
(b) Crashworthy structure for LH_2 tanks

Figure 19 – Structural integration concept

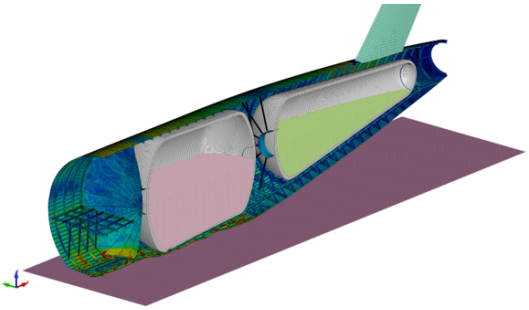
3.3.3 Response Under Vertical Loading

This section presents the structural response of the forward LH_2 tank across component, major component and full-scale levels under vertical loading as described in section 2.4.2. Symmetric boundary conditions (U_x = 0, R_y = 0, R_z = 0) were applied at the front end of the component and major component models to simulate full aircraft conditions. Figure 20 shows the von Mises equivalent stress distribution for the component, major component and full-scale models, respectively, at the time of maximum internal energy (t = 75 ms, 85 ms and 130 ms).

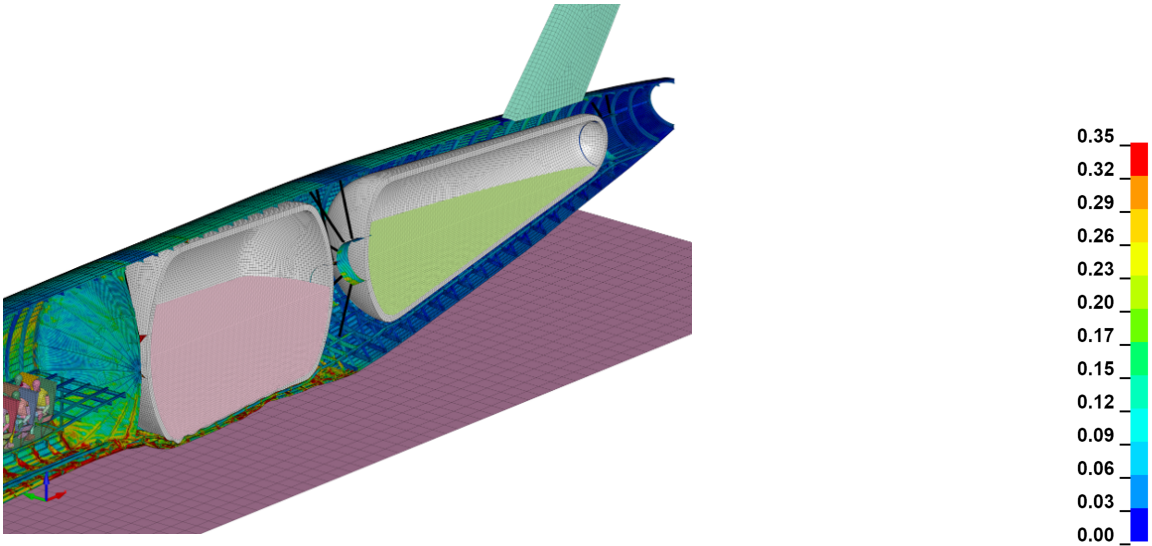
The sub-tank structure was designed based on loads derived from the component-level fuselage section, utilizing the full available crushing distance to minimize load transfer to the LH_2 tank's outer jacket. Accordingly, the curved crossbeams were dimensioned to withstand the crushing forces exerted by the sub-tank struts. However, deformations and loads on the sub-tank structure, the outer jacket, and the insulation increase significantly when transitioning from the component level to the major component and, ultimately, the full-scale level. This increase is primarily attributable to the substantially higher structural mass of the complete fuselage in the full-scale model. The fuselage region that contains the forward LH_2 tank is not only stressed by the mass of the fuselage from the



(a) Component level at t = 75 ms



(b) Major component level at t = 85 ms



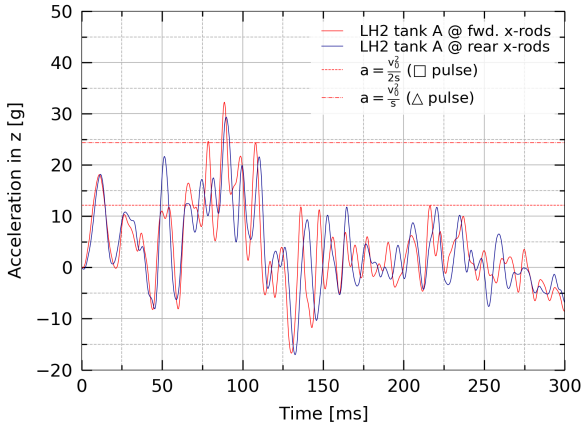
(c) Full-scale level at t = 130 ms

Figure 20 – von Mises equivalent stress distribution in GPa at maximum crushing displacement

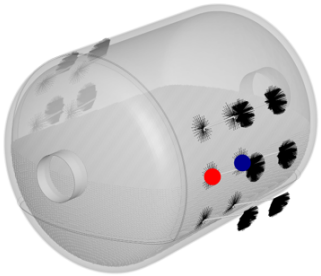
conical section on the rear edge, but also by the mass of the passenger cabin on the forward edge. Given that the cabin region exhibits a higher mass per frame than the tank compartment, and its cargo hold remains empty, the overall deformation of the sub-floor area is significantly more pronounced than that beneath the sub-tank structure. Consequently, the structural loads transmitted to the fuselage section containing the forward tank are amplified. To align the component level results with full-scale results, the fuselage section model must incorporate inertial effects on both edges in addition to the symmetric boundary conditions. The missing mass of the conical and cabin regions must be added to the rear and forward edges by applying equivalent line loads at these edges.

The tail section and the sub-tank structure of the rear tank exhibit minimal plastic deformation, as they are situated outside the primary crush zone. In contrast to the forward tank's crash structure, which undergoes significant structural deformation, the rear assembly remains largely stable. Based on these simulation results, the rear crash structure was optimized by reducing its mass to one-third of the original design, resulting in a total weight saving of 180 kg.

Figure 21 depicts the tank accelerations in global z-direction at lateral tank surface, with the evaluation nodes shown in Figure 21b, at full-scale level. The results on component and major component level are depicted in the appendix (Figure 28). The peak acceleration is about 32 g at the full-scale level. To facilitate preliminary design, these results are compared with idealized rectangular (12.2 g) and triangular (24.4 g) acceleration pulses, evaluated for an impact velocity of v_z = 9.14 m/s (30 ft/s) and a crushing distance of s = 350 mm. Despite the observed peaks, the measured acceleration values remain largely within the analytical bounds of the idealized pulse shapes. To improve the fidelity of these results, subsequent studies must incorporate detailed material properties and tank models to precisely determine the structural reaction. The inverse proportionality between acceleration and crushing distance underscores a critical design trade-off: reducing the minimum acceleration of 12.2 g by half would require doubling the crushing distance to 700 mm, resulting in a considerable impact on the overall aircraft.



(a) Full-scale level



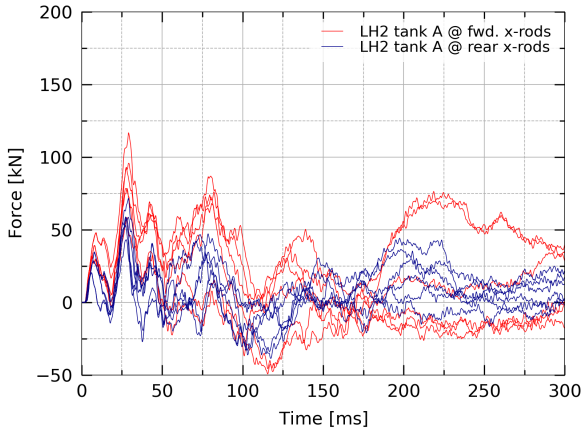
(b) Location of evaluation nodes

Figure 21 – Accelerations in z-direction at lateral tank surface (forward LH_2 tank)

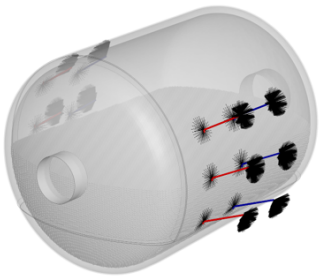
3.3.4 Response Under Horizontal-Dominated Loading

This section presents the structural response of the forward LH_2 tank at the full-scale level under horizontal-dominated loading as described in section 2.4.2.

Figure 22 compares the axial forces in the x-rods at full-scale level. The results for the component and major component level are depicted in the appendix (Figure 29). In general, the forward x-rods are subjected to significantly higher loads than the rear ones. A peak force of approximately 117 kN is measured at the full-scale level. The comparatively low loading of the rear x-rods indicates that a configuration with a single row of x-rods may be sufficient. The non-uniform loading of the forward x-rods is caused by their orientation. To achieve a more uniform load distribution among all x-rods and to reduce potential overloading of the surrounding structure, the integration of load limiters into the x-rods may be considered (e.g. energy absorption by progressive bearing failure [65]).



(a) Full-scale level



(b) Location of evaluation x-rods

Figure 22 – Axial forces in the x-rods (forward LH_2 tank)

Figure 23 shows the full-scale crash simulation with combined velocity components at four time points (t = 100 ms, 200 ms, 300 ms, 400 ms). The fuselage contour plot shows the von Mises stress in GPa, while the SPH particles are coloured by global x-velocity in m/s. The fuselage impacts the surface simultaneously along its full length. Most of the vertical kinetic energy is absorbed by plastic deformation of the fuselage while the spokes experience significant axial tensile forces. These forces cause noticeable deformation of the tank dome, especially in the forward tank (Figure 23 at t = 100 ms). As previously discussed for the x-rods, load limiters can be integrated into the spokes to prevent local overloading and to achieve a more uniform distribution of axial loads. This enables controlled deformation at a defined load level and reduces further load transfer to the surrounding

structure, including the tank dome and fuselage. The results demonstrate that the structure maintains its structural integrity under the specific applied load case, with no fuselage break occurring.

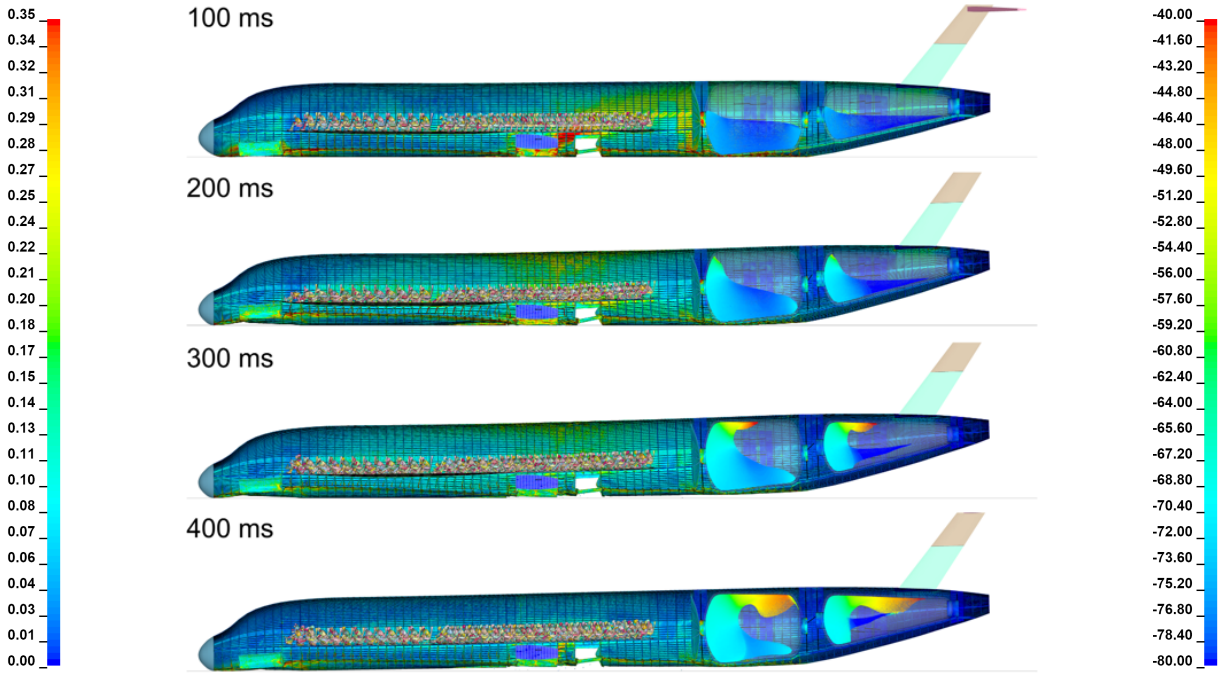


Figure 23 – Full-scale crash simulation with combined velocity components. The fuselage structure is shown with von Mises stress (GPa) and the SPH particles in the tanks are coloured by x-velocity (m/s)

4. Aircraft Design and Assessment of DLH25

The following chapter details the outcomes of the aircraft design process, providing a comprehensive overview of the resulting DLH25. The resulting data of the iterative aircraft design process including the component design studies are consolidated into a cohesive aircraft architecture, presenting the finalized conceptual aircraft design of the DLH25. A comparative analysis is subsequently performed in order to highlight the primary differences between the current design and its predecessor, with a particular focus on the influence of revised LH_2 technological assumptions. The chapter concludes with a quantitative comparison of the LH_2 concept with a technically equivalent SAF-powered aircraft, thereby providing a basis for evaluating the impact of hydrogen integration on overall aircraft performance.

4.1 Revision of previous assumptions

The integration of liquid hydrogen as an energy carrier constitutes a revolutionary shift in fuel storage concepts and thus poses a significant challenge to the conceptual aircraft design. There is a notable lack of established methodologies for the integration of cryogenic tanks and associated components. As a result, the previous conceptual investigation [19] was required to set technological assumptions for the utilisation of LH_2. The present study enables some of these approximations to be replaced by higher-fidelity analysis and simulation results, thereby increasing the maturity of the overall design. The key modifications to the existing technological assumptions for the aircraft design are summarized in Table 5.

With respect to engine performance, the preliminary assumption of a general 5% performance increase, attributed to the higher specific heat capacity of the exhaust gas, has been superseded by a new performance map derived from the LH_2 turbofan engine design, taking the thermodynamic cycle design and flow path sizing into account. Consequently, a generalized assessment of SEC performance is no longer pursued. Instead, the performance map enables the consideration of all operating states along the entire flight envelope, including off-design operating points. An analysis of the data

Component	*Technology Factor in [19]*	*Results*	*Rationale*
Engine Performance	+5%	Fully replaced *(Mid-Cr.: +3.3%)*	The engine performance benefit was replaced by a complete engine performance map.
Fuselage Mass	+7%	+1340 kg *(9%)*	Updated mass for crash structure. +1% for tank removal systems and access panels.
Spacing for Cold Box	1.5 m	1.05 m	Necessary geometrical spacing for cold box integration from detailed system design.
Mass for LH_2 systems (incl. LH_2/GH_2 pipes)	730 kg	1240 kg	Higher mass driven by specific mass for LH_2/ GH_2 pipes as depicted in Table 9.
Unusable Fuel Mass	10%	7%	Updated result from system design as depicted in Table 2.
Wing Mass	+5%	+5%	Compared to DLR-F25. No relief of wing structure due to dry wing.

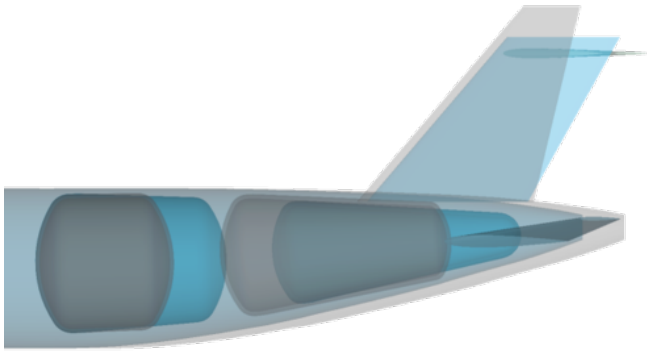
Table 5 – Updated results for previous technology assumptions applied during conceptual aircraft design phase of the DLH25

presented in Table 4 indicates that the LH_2 engine achieves a 3.3% reduction in thrust-specific energy consumption at the mid-cruise point compared to a technologically equivalent SAF-powered UHBR engine. While the mass of the tank integration and crash structure was previously estimated at 7% of the total fuselage mass, it can now be accurately quantified with 1340 kg (9% of fuselage mass). Additionally, a mass penalty of 1% of the fuselage mass is still assumed for tank removal systems and maintenance access panels. The detailed system design revealed that while the inter-tank spacing could be reduced from 1.5 m to 1.05 m, the total LH_2 system mass, including the LH_2/GH_2 piping, increases by 510 kg up to 1240 kg and the unusable fuel mass fraction can be set to 7%. For the wing structure, the assumption of a 5% mass increase for the dry wing is maintained being a potential objective for future detailed design studies.

4.2 Design Iteration DLH25

To refine the initial configuration, targeted investigations were conducted at the overall aircraft design level to identify potential improvements of the DLH25. Specifically, the transition from a conventional tail to a T-tail configuration eliminates the intersection of the horizontal stabilizer with the fuselage, thereby increasing the available volume for tank integration in the rear section, as can be seen in Figure 24. This reduces not only the fuselage mass but also decreases the wetted area and improves overall aircraft performance. The positioning increases the lever arm of the HTP and its aerodynamic efficiency due to reduced interference from downwash effects caused by the wing, allowing for a smaller HTP area. However, this configuration also necessitates consideration of increased structural mass and increased frame thickness required for T-tail integration. Simultaneously, the fuel distribution was optimized by allocating 70% of the total volume to the forward tank and 30% to the rear tank. The rear tank was narrowed to ensure sufficient clearance for the fuselage structure, particularly to accommodate the increased frame thickness required for the T-tail integration. This revised distribution reduces the surface-to-volume ratio (S/V) of the LH_2 tanks by 4.3%, thereby reducing the total structural mass leading to an increase of the strucutral gravimetric index of 1.8%. This mass reduction is attributed to both a decrease in the required wall material and a reduction in insulation thickness, as the diminished surface area lowers the overall heat ingress. The combination of these two modifications, the T-tail configuration and the revised volume distribution, enabled a reduction in total fuselage length by 2.7%. This shortening leads to a direct decrease in the overall CoG shift, the structural mass of the fuselage and its overall wetted area leading to an increase in fuel efficiency of 2.8%.

The DLH25 aircraft, consolidated from the results of the component design studies, is depicted in the three-view drawing in Figure 25. The required geometrical spacing for both the hydrogen systems and the tank crash structure are provided within the fuselage, with the resulting masses and CoG positions



Parameter	*Delta*
Fuselage Length	*-2.7%*
S/V Ratio	*-4.3%*
GI (structural)	*+1.8%*

Figure 24 – Tail section comparison between conventional (grey) and T-tail (blue) configuration including different tank volume distributions

fully accounted for. Furthermore, the UHBR-LH_2 engine, considering the required heat flows for LH_2 pre-conditioning, was integrated into the overall configuration by incorporating the corresponding mass, geometry, and performance map. The key parameters of the resulting DLH25 including a MEM- and a drag-breakdown are summarized and compared to the previous DLH25 concept in Table 7 and Figure 26.

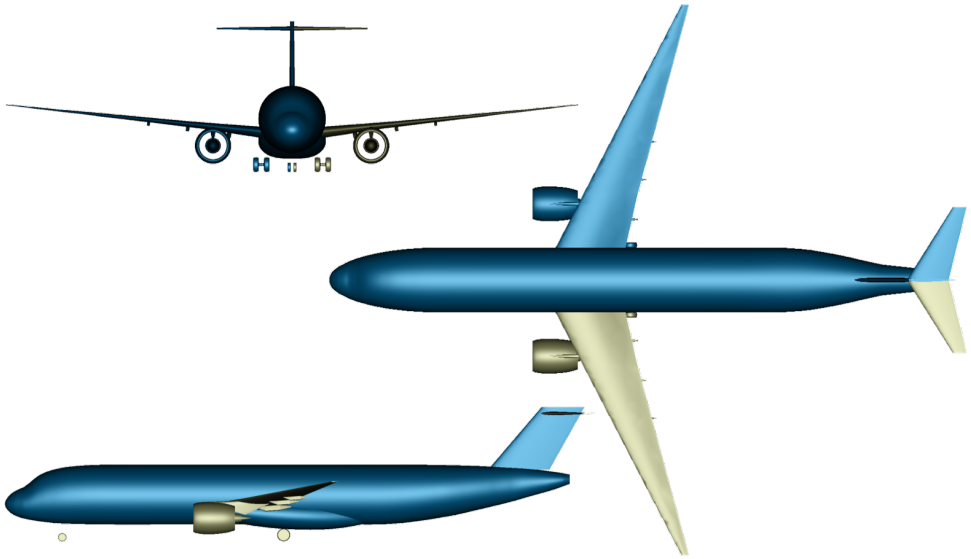


Figure 25 – Three-View of the updated DLH25

The results indicate that the OEM of the updated DLH25 is reduced by 2.7%, which consequently leads to a 2.1% reduction in MTOM. This mass reduction is attributable to several factors illustrated in the MEM mass breakdown (Figure 26a). Firstly, the engine designed for LH_2 combustion proved to be lighter than initially assumed, with its mass decreasing from 8870 kg to 8090 kg. Furthermore, the aero-engine matching for the take-off performance was optimized. A reduction of the take-off lift coefficient $c_{L,TO}$ to 1.9 resulted in a higher lift-off speed and thus, higher rotation speed, to satisfy the requirement of a balanced field length of 2200 m. This increased the dynamic pressure at the HTP allowing for a smaller HTP design, as its dimensions were previously sized by the take-off rotation requirement. This modification resulted in a mass saving of 380 kg and a reduction in zero-lift drag ($c_{d,0}$) by 7 drag counts (26b). The fuselage mass remained nearly constant, as mass savings from the modified tail configuration were offset by an increased mass requirement for the crash concept. Due to the overall weight reduction of the DLH25, the maximum landing mass (MLM) is also lowered. This parameter is decisive for the sizing of the wing area, given the constant wingspan and the specified TLAR criterion of an approach speed of 136 kts. Thus, the aspect ratio increases by 3.1%, which, combined with the reduced wetted area of a shorter fuselage and a smaller HTP, enhances the aerodynamic efficiency. Consequently, the L/D ratio increases by 4.6% for the evaluation mission

Key Sizing Parameters	Unit	DLH25 [19] (initial)	DLH25 (update)	*Delta [%]*
W/S = MTOM/Sref	kg/m^2	591	590	*-0.2*
T/W = SLST/MTOM	-	0.330	0.319	*-3.3*
Masses				
Max. Take-Off Mass	t	93.4	91.4	*-2.1*
Max. Landing Mass	t	88.3	86.5	*-2.0*
Max. Zero Fuel Mass	t	87.0	85.3	*-2.0*
Operating Empty Mass	t	62.0	60.3	*-2.7*
Max. Fuel Mass	t	6.5	6.1	*-6.2*
Block Fuel (2500 NM)	t	5.4	5.1	*-5.4*
Block Energy (2500 NM)	GJ	643	608	*-5.4*
Block Energy (800 NM)	GJ	228	214	*-6.1*
Geometry				
Wing Span	m	45	45	*0.0*
Wing Aspect Ratio	-	12.8	13.1	*+2.3*
Wing MAC	m	4.26	4.2	*-1.4*
Wing Ref. Area	m^2	158	155	*-1.9*
Fuselage Length	m	51.4	49.7	*-3.3*
Propulsion				
Equivalent static thrust (SL/ISA)	kN	152	143	*-5.9*
TSEC cruise average (800 NM)	MJ/s/kN	0.588	0.599	*+1.8*
Aerodynamic				
$c_{L,cruise}$ (800 NM)	-	0.58	0.58	*0.0*
$L/D_{cruise,\ average}$ (800 NM)	-	17.5	18.3	*+4.6*
$c_{L,max,TO}$	-	2.1	1.9	*-9.5*
$c_{L,max,L}$	-	2.76	2.76	*0.0*

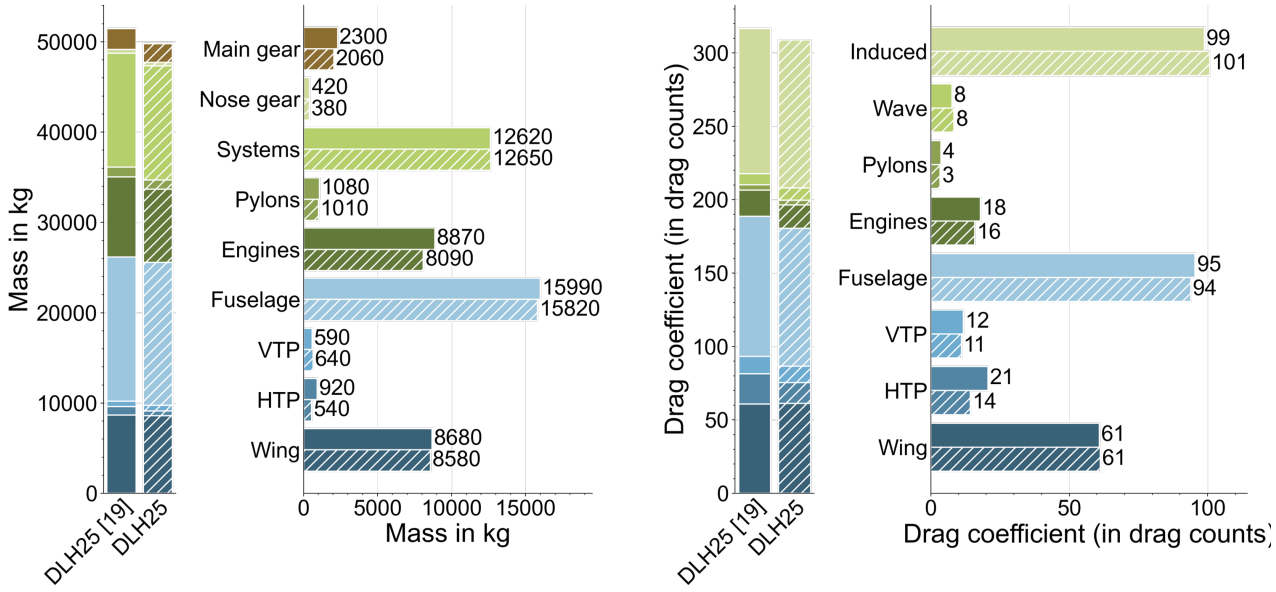
Table 7 – Key characteristic parameter of the initial DLH25[19] and the updated DLH25

(800 nautical miles, 22705 kg payload). Although the engine is on average 1.8% less efficient during the cruise phase of the evaluation mission than its predecessor, the overall efficiency of the DLH25 increases by 6.1%.

4.3 Performance comparison to a SAF powered Research Baseline

To contextualize the updated DLH25 hydrogen concept and its resulting performance, the DLH25 is compared in the following step with the reference configuration D239 (technology level 2020), as well as with the DLR-F25, a SAF research baseline equivalent to the 2035 technology level. Initially, the geometric differences between the DLH25 and the DLR-F25 are illustrated in the three-view drawing in Figure 27. It is evident that the DLH25 exhibits both a larger fuselage diameter (5.3 m) and a longer fuselage (49.7 m) than the DLR-F25, despite the fuselage shortening resulting from the T-tail. Due to the unswept trailing edge of the wings, both concepts employ a body-mounted landing gear. The wingspan is initially maintained at 45.0 m to ensure a consistent length of the foldable wing tip, thereby ensuring compliance with the 36.0 m gate limit.

The key characteristics of the D239, DLR-F25, and DLH25 are compared in Table 8, with the following analysis focusing specifically on the DLR-F25 and DLH25. The increase of 30.2% in OEM for the DLH25 is primarily attributed to the integration of liquid hydrogen tanks and systems, and the necessary crash structure. The 63.5% reduction in fuel mass limits the overall increase in MTOM to 6.7%. However, the disparity in energy density and the resulting fuel mass lead to a 16.6% increase



(a) MEM Breakdown

(b) Drag Breakdown

Figure 26 – MEM and drag breakdown comparisons for the initial DLH25 [19] (solid) and the updated DLH25 (hatched)

in MLM. Given the approach speed constraints (TLAR) and a constant wingspan, this necessitates an increase in wing area, which reduces the aspect ratio by -16.0% and consequently impairs the aerodynamic efficiency of the DLH25. A comprehensive aero-structural optimization of the wingspan for both concepts remains a compelling objective for future research. For the evaluation mission, the aerodynamic performance drops from an L/D of 19.5 to 18.3. Conversely, the TSEC of the DLH25 is improved by 3.1%, a result of the transition to hydrogen combustion. Compared to the DLR-F25, the DLH25 exhibits an increase in block energy of 16.5% for the design mission and 20.2% for the evaluation mission. In contrast, when compared to the D239, the DLH25 achieves a reduction in block energy consumption of 6.0% and 1.0% for the design and evaluation missions, respectively. Notably,

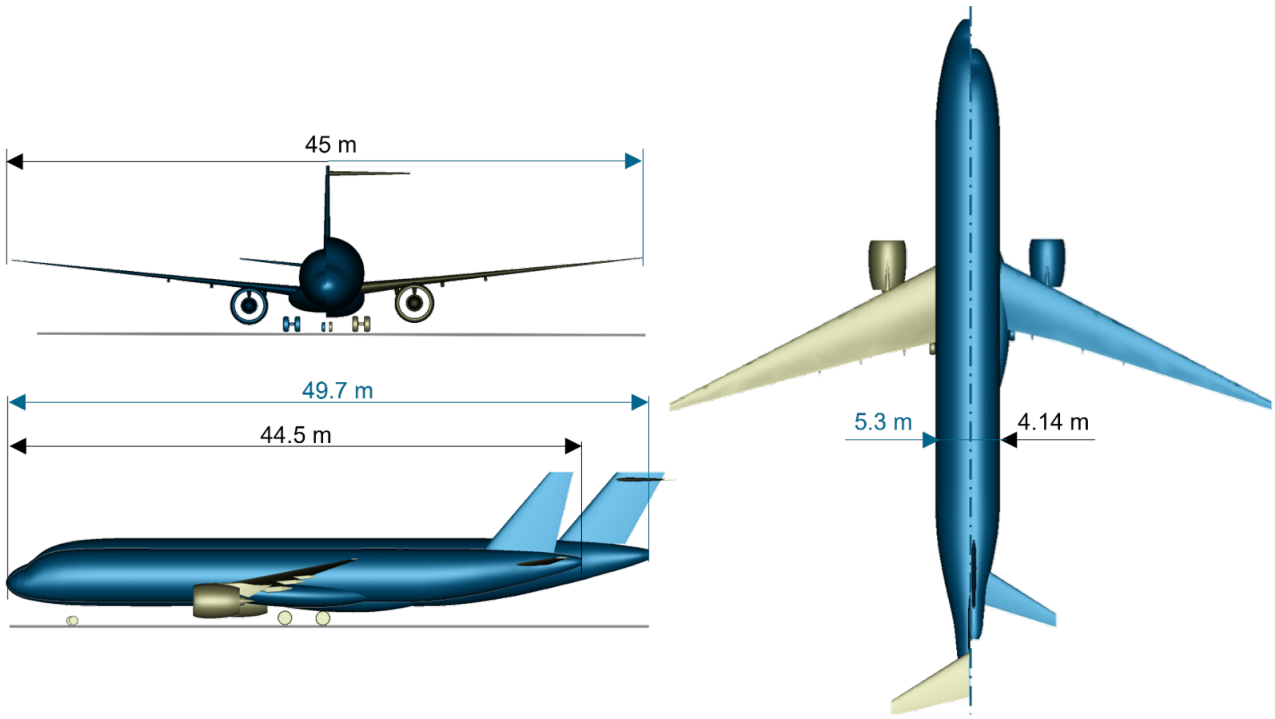


Figure 27 – Three-View comparison of the DLR-F25 (blue) and the DLH25 (yellow)

the efficiency of the LH_2 aircraft degrades more rapidly than that of the SAF aircraft when operating in off-design points. This performance gap is attributed to the higher OEM, due to the structural mass of the hydrogen storage systems, combined with a smaller fuel mass delta, which penalizes off-design range deviations more heavily.

This result underscores the current technical challenges associated with the integration of liquid hydrogen storage into an aircraft design. However, prior research indicates that LH_2-powered aircraft exhibit a higher sensitivity to efficiency alterations compared to SAF powered aircraft. Specifically, Kugler et al. [66] demonstrated that the integration of revolutionary technologies on LH_2 powered aircraft, such as the Truss-Braced Wing or Open Fan architectures, yields more pronounced efficiency improvements than their SAF equivalents, thereby potentially narrowing the existing performance gap. Furthermore, Silberhorn et al. [67, 68] identified potential for further efficiency enhancements through the implementation of mild hybridization via fuel cell integration, a technological pathway that offers significantly fewer synergies for SAF configurations, as they lack an onboard hydrogen source. Consequently, it is imperative that future evaluations adopt a holistic approach, extending the analysis beyond pure block energy efficiency to include direct operating costs (DOC) and climate impact parameters. Ultimately, by systematically addressing the integration challenges of LH_2, this study reinforces the position of liquid hydrogen as a viable energy carrier for the long-term decarbonization of the aviation sector. Furthermore, these results indicate that continued research and further detailed investigations, as demonstrated in this study, hold potential for additional efficiency improvements.

Key Sizing Parameters	**Unit**	**D239**	**DLR-F25**	**DLH25**	*Delta to D239 [%]*	*Delta to DLR-F25 [%]*
W/S = MTOM/Sref	kg/m^2	720	659	590	*-18.1*	*-10.5*
T/W = SLST/MTOM	-	0.319	0.296	0.319	*0.0*	*+7.8*
Masses						
Max. Take-Off Mass	t	93.5	85.7	91.4	*-2.2*	*+6.7*
Max. Landing Mass	t	79.2	74.2	86.5	*+9.2*	*+16.6*
Max. Zero Fuel Mass	t	75.6	71.3	85.3	*+12.8*	*+19.6*
Operating Empty Mass	t	50.6	46.3	60.3	*+19.2*	*+30.2*
Max. Fuel Mass	t	18.4	16.7	6.1	*-66.8*	*-63.5*
Block Fuel (2500 NM)	t	15.0	12.1	5.1	*-66.0*	*-57.9*
Block Energy (2500 NM)	GJ	647	522	608	*-6.0*	*+16.5*
Block Energy (800 NM)	GJ	216	178	214	*-1.0*	*+20.2*
Geometry						
Wing Span	m	36	45	45	*25.0*	*0.0*
Wing Aspect Ratio	-	9.9	15.6	13.1	*+32.3*	*-16.0*
Wing MAC	m	4.3	3.54	4.2	*-2.3*	*+18.6*
Wing Ref. Area	m^2	130	130	155	*+19.2*	*+19.2*
Fuselage Length	m	44.51	44.51	49.7	*+11.7*	*+11.7*
Propulsion						
Equivalent static thrust (SL/ISA)	kN	147	125	143.0	*-2.7*	*+14.4*
TSEC cruise average (800 NM)	MJ/s/kN	0.643	0.618	0.599	*-6.9*	*-3.1*
Aerodynamic						
$c_{L,cruise}$ (800 NM)	-	0.581	0.593	0.58	*-0.2*	*-2.2*
$L/D_{cruise,\ average}$ (800 NM)	-	17.5	19.5	18.3	*+4.6*	*-6.2*
$c_{L,max,TO}$	-	2.4	2.3	1.9	*-20.8*	*-17.4*
$c_{L,max,L}$	-	3.05	2.845	2.76	*-9.5*	*-3.0*

Table 8 – Key characteristic parameter comparison between D239, DLR-F25 and DLH25

5. Conclusion and Outlook

The present study has enhanced the design maturity of the DLH25 research baseline by integrating component design data into the preliminary design process and re-evaluating initial technological assumptions. The resulting updated baseline provides a robust foundation for subsequent research into the integration of next-generation technologies. A key contribution of this work was the integration of an LH_2-UHBR engine, considering the necessary heat flow for the hydrogen pre-conditioning system. When compared to a technologically equivalent SAF-powered engine, the LH_2 variant is 8.9% heavier. However, it achieves a 3.3% reduction in specific energy consumption at the mid-cruise point, correcting the previously assumed improvement of 5.0%. On a system level, the on-board and LH_2 systems exhibit a mass increase of 75% relative to a SAF aircraft, with the structural and crashworthy integration of the LH_2 tanks contributing a mass penalty of 1340 kg. To mitigate these challenges, configurational optimizations were implemented, including the transition to a T-tail to increase volumetric capacity and optimize fuel distribution. These changes resulted in a 2.8% improvement in block fuel efficiency, contributing to an overall increase of 6.0% compared to the predecessor of the DLH25. When compared to the DLR-F25 SAF research baseline, the DLH25 exhibits an increase in block energy of 16.5% for the design mission and 20.2% for the evaluation mission. Conversely, it demonstrates a superior block energy efficiency to the current state-of-the-art kerosene reference aircraft by 6.0% on the design mission and 1.0% on the evaluation mission.
Future research will focus on optimizing the interface between the LH_2 tanks and the crash structure to establish more precise sizing criteria and including additional load cases. Furthermore, the integration of novel technologies, such as Truss-Braced Wing and Open Fan architectures, and a comprehensive assessment of direct operating costs (DOC) and climate impact relative to SAF will be conducted. To further increase the technological maturity of the concept, detailed CFD analyses will be performed to evaluate the trim drag impact for the larger shift on CoG compared to the SAF aircraft. Additionally, the aero-structural behavior of the wing and a wingspan trade-off study, including a comparison with the SAF baseline, represent potential areas for further investigation.

6. Contact Author Email Address

Michael Kotzem
German Aerospace Center (DLR)
Institute of System Architectures in Aeronautics, Hamburg, Germany
mailto: michael.kotzem@dlr.de

7. Copyright Statement

The authors confirm that they, and/or their company or organization, hold copyright on all of the original material included in this paper. The authors also confirm that they have obtained permission, from the copyright holder of any third party material included in this paper, to publish it as part of their paper. The authors confirm that they give permission, or have obtained permission from the copyright holder of this paper, for the publication and distribution of this paper as part of the ICAS proceedings or as individual off-prints from the proceedings.

8. Acknowledgements

The Short-Medium Range Aircraft Architecture And Technology Integration Project (SMR ACAP, project number: 101101955) is supported by the Clean Aviation Joint Undertaking and its members. Disclaimer: Funded by the European Union. Views and opinions expressed are however those of the author(s) only and do not necessarily reflect those of the European Union or Clean Aviation Joint Undertaking. Neither the European Union nor the granting authority can be held responsible for them.





Co-funded by
the European Union

The authors would like to thank the German Aerospace Center (DLR) for providing the DLR-F25 test case. The development of the DLR-F25 configuration is funded by the German Federal Ministry for Economic Affairs and Climate Action (BMWK) as part of the LuFo VI-2 project VIRENFREI (funding reference: 20X2106B).

Supported by:



on the basis of a decision
by the German Bundestag

References

[1] European Commission and Directorate-General for Mobility and Transport and Directorate-General for Research and Innovation. *Flightpath 2050 – Europe's vision for aviation – Maintaining global leadership and serving society's needs*. Publications Office, 2011.

[2] Dries Verstraete. Long range transport aircraft using hydrogen fuel. *International Journal of Hydrogen Energy*, 38(34):14824–14831, 2013.

[3] Jona Eissele, Stefan Lafer, Cristian Mejía Burbano, Julian Schließus, Tristan Wiedmann, Jonas Mangold, and Andreas Strohmayer. Hydrogen-powered aviation—design of a hybrid-electric regional aircraft for entry into service in 2040. *Aerospace*, 10(3), 2023.

[4] Sebastian Wöhler, Tim Burschyk, Jannik Häßy, and Michael Iwanizki. Design and assessment of long-range aircraft concepts with focus on fossil kerosene, sustainable aviation fuel and liquid hydrogen as energy carriers. In *AIAA Aviation and Aeronautics Forum and Exposition, AIAA AVIATION Forum 2023*, Juli 2023.

[5] Vittorio Cipolla, Davide Zanetti, Karim Abu Salem, Vincenzo Binante, and Giuseppe Palaia. A parametric approach for conceptual integration and performance studies of liquid hydrogen short–medium range aircraft. *Applied Sciences*, 12(14), 2022.

[6] Carlos Xisto and Anders Lundbladh. Design and performance of liquid hydrogen fuelled aircraft for year 2050 eis. In *33rd congress of the international council of the aeronautical sciences*, volume 2, pages 1119–31. ICAS, 2022.

[7] Stanislav Karpuk, Yiyuan Ma, and Ali Elham. Design investigation of potential long-range hydrogen combustion blended wing body aircraft with future technologies. *Aerospace*, 10(6), 2023.

[8] Felix Fritzsche, Daniel Silberhorn, Vincenzo Nugnes, Tim Burschyk, and Michael Kotzem. Advancements in liquid hydrogen aircraft configuration design and assessment. *Engineering Proceedings*, 133(1), 2026.

[9] G. Onorato, P. Proesmans, and M. F. M. Hoogreef. Assessment of hydrogen transport aircraft. *CEAS Aeronautical Journal*, 13(4):813–845, 2022.

[10] G. Daniel Brewer. *Hydrogen Aircraft Technology*. CRC Press, 1991.

[11] Arturo Gomez and Howard Smith. Liquid hydrogen fuel tanks for commercial aviation: Structural sizing and stress analysis. *Aerospace Science and Technology*, 95:105438, 2019.

[12] Sergio Bagarello, Dario Campagna, and Ivano Benedetti. Computational thermo-mechanical modelling and design-space exploration of cryogenic hydrogen tanks for aviation. *Aerospace Science and Technology*, 168:110755, 2026.

[13] Musavir Bashir, Gala Licheva, and Susan Liscouët-Hanke. Transient boil-off and pressure dynamics analysis in aircraft liquid hydrogen tanks. *Aerospace Science and Technology*, 174:111887, 2026.

[14] Jingfa Li, Chaoyang Fan, Zhibo Chen, Huijie Huang, Kaiqiang Feng, Bo Yu, and Jiang Bian. Numerical study on the thermodynamic characteristics of liquid hydrogen storage tank sloshing in hydrogen-fueled civil aircraft. *Applied Thermal Engineering*, 299:131139, 2026.

[15] Linus Kameni Monkam, Arne Graf von Schweinitz, Jens Friedrichs, and Xin Gao. Feasibility analysis of a new thermal insulation concept of cryogenic fuel tanks for hydrogen fuel cell powered commercial aircraft. *International Journal of Hydrogen Energy*, 47(73):31395–31408, 2022.

[16] Maria Cristina Cameretti, Roberta De Robbio, Vincenzo Ferrara, and Raffaele Tuccillo. Performance and emissions evaluation of a turbofan burner with hydrogen fuel. *Aerospace*, 12(3), 2025.

[17] Swapnil S. Jagtap, Peter R.N. Childs, and Marc E.J. Stettler. Conceptual design-optimisation of a future

hydrogen-powered ultrahigh bypass ratio geared turbofan engine. *International Journal of Hydrogen Energy*, 95:317–328, 2024.

[18] Andrea Ballotti. *High-fidelity numerical modeling and design of hydrogen burners for aero engine applications*. Phd thesis, 2025.

[19] Michael Kotzem, Sebastian Wöhler, Tim Burschyk, Christian Hesse, Sven Hellbrück, and Thomas Zill. Conceptual aircraft design of a research baseline with direct liquid hydrogen combustion. In *34th Congress of the International Council of the Aeronautical Sciences (ICAS)*, 2024.

[20] Sebastian Wöhler, Jannik Häßy, and Vivian Kriewall. Establishing the dlr-f25 as a research baseline aircraft for the short-medium range market in 2035. In *34rd Congress of the International Council of the Aeronautical Sciences (ICAS)*, Florence, Italy, 2024.

[21] Sebastian Wöhler, Georgi Atanasov, Daniel Silberhorn, Benjamin Fröhler, and Thomas Zill. Preliminary aircraft design within a multidisciplinary and multifidelity design environment. In *Aerospace Europe Conference 2020*, 2020.

[22] Brigitte Boden, Jan Flink, Niklas Först, Robert Mischke, Kathrin Schaffert, Alexander Weinert, Annika Wohlan, and Andreas Schreiber. Rce: An integration environment for engineering and science. *SoftwareX*, 15:100759, 2021.

[23] Marko Alder, Erwin Moerland, Jonas Jepsen, and Björn Nagel. Recent advances in establishing a common language for aircraft design with cpacs. In *Aerospace Europe Conference 2020*, 2020.

[24] Nils Kuelper, Jasmin Broehan, Thimo Bielsky, and Frank Thielecke. Systems Architecting Assistant (SArA) - Enabling A Seamless Process Chain from Requirements to Overall Systems Design. In *33rd Congress of the International Council of the Aeronautical Sciences, ICAS*, Stockholm, Sweden, 2022.

[25] Thimo Bielsky, Nils Kuelper, and Frank Thielecke. Overall Parametric Design and Integration of On-Board Systems for a Hydrogen-Powered Concept Aircraft. In *Aerospace Europe Conference AEC*. EUCASS-CEAS, 2023.

[26] Vivian Kriewall, Marc Juenemann, and Frank Thielecke. Engine cycle adaptation method for aircraft on-board systems evaluation considering system-engine interaction. In *AIAA Science and Technology Forum and Exposition (AIAA SciTech Forum)*, Orlando, USA, 2024.

[27] Tim Burschyk, Marko Alder, Andrea Mancini, Thimo Bielsky, Vivian Kriewall, Frank Thielecke, and Björn Nagel. Introduction of a system definition in the common parametric aircraft configuration schema (cpacs). *Aerospace*, 12(5), 2025.

[28] Thimo Bielsky, F. Thielecke, G. Atanasov, T. Burschyk, and B. Nagel. Collaborative Parametric Overall Aircraft and Systems Design to Evaluate Hydrogen-Powered Regional Aircraft. In *German Aerospace Congress*, Hamburg, Germany, September 2024. German Society for Aeronautics and Astronautics - Lilienthal-Oberth e.V.

[29] Fabian Nicolas Peter, Marc Engelmann, Meriem Fikry, Michael Lüdemann, Leonard Moser, Christopher Warsch, Rafael Balderas-Xicohtencatl, Adnan Muslić, Elif Erden, Mirko Hornung, Tobias Welsch, Florian Schültke, Eike Stumpf, Samarth Kakkar, Wolfgang Heinze, Matthias Haupt, Rolf Radespiel, Vivian Kriewall Peters, Thimo Bielsky, Frank Thielecke, Nicolas Moebs, and Andreas Strohmayer. Results of the H2Avia Project: Potential of Hydrogen for Global Aviation. *Aerospace*, 13(6):550, June 2026.

[30] Nils Kuelper, Thimo Bielsky, Jasmin Broehan, and Frank Thielecke. Model-Based Framework for Data and Knowledge-Driven Systems Architecting Demonstrated on a Hydrogen-Powered Concept Aircraft. *INSIGHT*, 27:47–60, March 2024.

[31] Nils Kuelper, Vivian Kriewall Peters, Kai Beschorner, and Frank Thielecke. TechMAPS: technology management for the architecting process of aircraft on-board systems. *CEAS Aeronautical Journal*, October 2025.

[32] Nils Kuelper, Andrew Jeyaraj, Susan Liscouet-Hanke, and Frank Thielecke. Integration of a Model-Based Systems Engineering Framework with Safety Assessment for Early Design Phases: A Case Study for Hydrogen-Based Aircraft Fuel System Architecting. *Results in Engineering*, 25:104249, February 2025.

[33] Nils Kuelper, Dennis Hillig, Jasmin Broehan, Lukas Stigge, and Frank Thielecke. Early Model-Based Functional Integration Testing for Aircraft Systems Architectures Demonstrated on a Hydrogen-Powered Propulsion Unit. Paris, October 2025.

[34] Thimo Bielsky, Marc Juenemann, and Frank Thielecke. Parametric Modeling of the Aircraft Electrical Supply System for overall Conceptual Systems Design. In *German Aerospace Congress*. German Society for Aeronautics and Astronautics - Lilienthal-Oberth e.V., 2021.

[35] Marc Juenemann, Thimo Bielsky, Vivian Kriewall, and Frank Thielecke. Overall Systems Design Method for Evaluation of Electro-Hydraulic Power Supply Concepts for Modern Mid-Range Aircraft. In *American Institute of Aeronautics and Astronautics (AIAA) Aviation Forum*, Chicago, USA, June 2022.

[36] Thimo Bielsky, Nils Kuelper, and Frank Thielecke. Assessment of an Auto-Routing Method for Topology Generation of Aircraft Power Supply Systems. In *German Aerospace Congress*, Dresden, Germany, September 2022. German Society for Aeronautics and Astronautics - Lilienthal-Oberth e.V.

[37] Julian Schicker, Vivian Kriewall Peters, and Frank Thielecke. Parametric Conceptual Design of Aircraft On-Board Liquid Hydrogen Storage and Supply Systems. 2026. In the process of publication.

[38] Tim Burschyk, Yannic Cabac, Daniel Silberhorn, Brigitte Boden, and Björn Nagel. Liquid hydrogen storage design trades for a short-range aircraft concept. *CEAS Aeronautical Journal*, 14(4):879–893, October 2023.

[39] W. C. Strack. Preliminary Performance Appraisal of Navy V/STOL Transport and Search-Type Airplanes Using Hydrogen Fuel. Technical Memorandum NASA-TM-X-71550, Ohio, May 1974.

[40] Richard-Gregor Becker, Stanislaus Reitenbach, Carsten Klein, Tom Otten, Mobin Nauroz, and Martin Siggel. An integrated method for propulsion system conceptual design. In *Proceedings of the ASME Turbo Expo: Turbine Technical Conference and Exposition - 2015*, New York, NY, 2015. ASME.

[41] Stanislaus Reitenbach, Alexander Krumme, Thomas Behrendt, Markus Schnös, Thomas Schmidt, Sandrine Hönig, Robert Mischke, and Erwin Mörland. Design and application of a multidisciplinary predesign process for novel engine concepts. *Journal of Engineering for Gas Turbines and Power*, 141(1), 2019.

[42] Stanislaus Reitenbach, Maximilian Vieweg, Richard Becker, Carsten Hollmann, Florian Wolters, Jens Schmeink, Tom Otten, and Martin Siggel. Collaborative aircraft engine preliminary design using a virtual engine platform, part a: Architecture and methodology. In *AIAA Scitech 2020 Forum*, Reston, Virginia, 01062020. American Institute of Aeronautics and Astronautics.

[43] *Step-by-Step Evaluation of the Fuel Switch From Kerosene to Hydrogen on the Thermodynamic Cycle in Gas Turbine Engines*, volume Volume 1: Aircraft Engine of *Turbo Expo*, 06 2024.

[44] Jannik Häßy and Jens Schmeink. Knowledge-based conceptual design methods for geometry and mass estimation of rubber aero engines. In *ICAS 2022 - 33rd Congress of the International Council of the Aeronautical Sciences*, Stockholm, Sweden, 2022.

[45] Jannik Häßy and Benjamin Fröhler. *The Virtual Propulsion Expert: Application of a Hybrid Surrogate-Based Rubber Engine Model in Aircraft Design*.

[46] Jannik Häßy, Martin Bolemant, and Richard-Gregor Becker. An Educated Guess - Predicting Turbomachinery Efficiencies of Aero Engines During Conceptual Design. volume Volume 1: Aircraft Engine of *Turbo Expo: Power for Land, Sea, and Air*, page V001T01A033, 06 2023.

[47] Matthias Waimer, Paul Schatrow, Erik Wegener, Nathalie Toso, and Heinz Voggenreiter. Crashworthiness considerations for liquid hydrogen tank integration in transport airplanes. *CEAS Aeronautical Journal*, 2025.

[48] Federal Aviation Administration. Special conditions: Boeing model 787-8 airplane; crashworthiness. Technical Report Docket No. NM368, Special Conditions No. 25–07–05–SC, 2007.

[49] Federal Aviation Administration. Special conditions: Airbus model A350-900 airplane; crashworthiness. Technical Report Docket No. FAA–2013–0892, Notice No. 25–13–21–SC, 2014.

[50] Justin D. Littell. A summary of results from two full-scale Fokker F28 fuselage section drop tests. Technical Report NASA/TM–2018-219829, NASA, 2018.

[51] Karen E. Jackson and Jacob B. Putnam. Development of a full-scale finite element model of the Fokker F28 Fellowship aircraft and crash simulation predictions. Technical report, NASA, 2020.

[52] European Union Aviation Safety Agency (EASA). Certification specifications for Large Aeroplanes (CS-25), 2026.

[53] Richard Johnson and Barry Wade. Longitudinal impact test of a transport airplane section. Technical Report DOT/FAA/CT-87/26, Federal Aviation Administration Technical Center, Atlantic City, NJ, 1988.

[54] Darrell Ault. Longitudinal acceleration test of overhead luggage bins in a transport airframe section. Technical Report DOT/FAA/CT-92/9, Federal Aviation Administration Technical Center, Atlantic City, NJ, 1992.

[55] Robert McGuire and Tim Macy. Longitudinal acceleration tests of overhead luggage bins and auxiliary fuel tank in a transport airplane airframe section. Technical Report DOT/FAA/AR-99/4, Federal Aviation Administration Technical Center, Atlantic City, NJ, 1999.

[56] Robert McGuire. Longitudinal acceleration test of overhead luggage bins and auxiliary fuel tank in a transport airplane airframe section, part II. Technical Report DOT/FAA/AR-99/4,II, Federal Aviation Administration Technical Center, 2000.

[57] Gil Wittlin and Bill LaBarge. KRASH dynamics analysis modeling – transport airplane controlled impact demonstration test. Technical Report DOT/FAA/CT-85/9, Federal Aviation Administration Technical Center, 1985.

[58] Michael Petsch, Dieter Kohlgrüber, and Jörg Heubischl. Pandora - a python based framework for modelling and structural sizing of transport aircraft. In *MATEC Web of Conferences*, volume 223 of *8th EASN – CEAS International Workshop Proceeding*, pages 1–8. MATEC Web of Conferences, November 2018.

[59] Paul Schatrow, Michael Petsch, Matthias Waimer, Nina Wegener, Christian Xavier Leon Muñoz, and Dieter Kohlgrüber. Method development for full aircraft crash simulation. In *The Tenth Triennial International Aircraft Fire & Cabin Safety Research Conference*, Atlantic City, New Jersey, USA, October 2022. October 17–20, 2022.

[60] Hao Ma, Xiaoyang Zheng, Xuan Luo, Yong Yi, and Fan Yang. Simulation and analysis of mechanical properties of silica aerogels: From rationalization to prediction. *Materials*, 11(2):214, 2018.

[61] Nathalie Renée Solange Toso. *Contribution to the Modelling and Simulation of Aircraft Structures Impacting on Water*. Thesis, 2009.

[62] Dieter Kohlgrüber, Christian Leon Muñoz, Michael Petsch, Paul Schatrow, and Matthias Waimer. Steps towards a numerical process chain to evaluate fuselage structural loads caused by sloshing in liquid hydrogen tanks. In *Aerospace Structural Impact Dynamics International Conference (ASIDIC 2025)*.

[63] Clean Aviation Joint Undertaking. FASTER H2 – Fuselage, Rear Fuselage and Empennage with Cabin and Cargo Architecture Solution Validation and Technologies for H_2 Integration, 2026. https://clean-aviation.eu/research-and-innovation/clean-aviation/clean-aviation-projects/faster-h2. Accessed: 17 March 2026.

[64] German Aerospace Center (DLR). FASTER H2: Key Technologies for Climate-Neutral Short- and Medium-Haul Aircraft, 2026. Accessed: 17 March 2026.

[65] Thomas Feser, Jazib Hassan, Matthias Waimer, Ronan M. O'Higgins, Conor T. McCarthy, Nathalie Toso, Heinz Voggenreiter, and Michael A. McCarthy. Effects of transient dynamic loading on the energy absorption capability of composite bolted joints undergoing extended bearing failure. *Composite Structures*, 247:112476, 2020.

[66] Lucas Kugler, Michael Alexander Kotzem, Sebastian Wöhler, and Thomas Zill. Assessing synergies between truss-braced wings, liquid hydrogen propulsion, and open rotors in conceptual aircraft design. Presented at *10th CEAS Aerospace Europe Conference* and in press to be published by *Materials Research Forum LLC*, 2025.

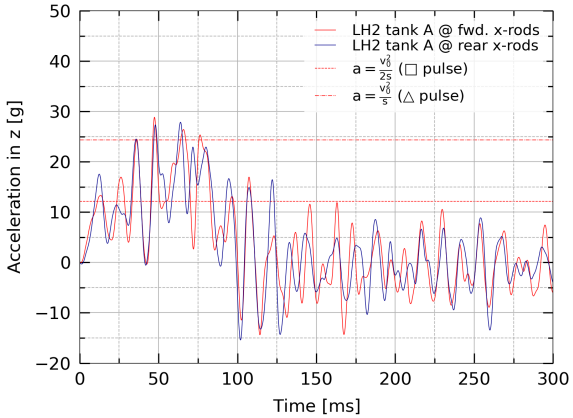
[67] Daniel Silberhorn, Tim Burschyk, Matthias Schroeder, and Georgi Atanasov. Potentials of hydrogen powered short-range aircraft concepts with mild-hybrid-electric propulsion architectures. Presented at the 15th EASN International Conference, 2025.

[68] Georgi Atanasov and Daniel Silberhorn. Hybrid aircraft for improved off-design performance and reduced emissions. In *AIAA 2020-0753. AIAA Scitech 2020 Forum. January 2020.*

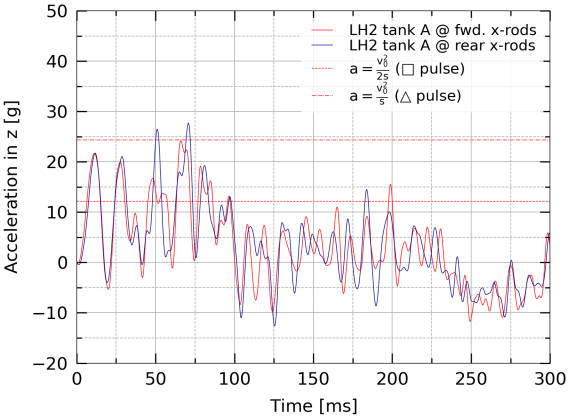
9. Appendix

Parameter	**Unit**	**LH_2 tank forward**	**LH_2 tank aft**
Outer bigger diameter	m	4.6	3.4
Outer smaller diameter	m	4.14	1.5
Insulation thickness	m	0.14	0.15
Inner wall thickness	mm	7.0	5.0
Length	m	6.3	8.2
Inner volume	m^3	71.4	30.6
Mass	kg	3350	1820
Parameter	**Unit**	**Cold box forward**	**Cold box aft**
Outer diameter	m	1.84	1.84
Inner diameter	m	1.63	1.63
Shell wall thickness	mm	3.5	3.5
Length	m	0.72	0.72
Separation betw. tanks	m	1.05	1.05
Mass	kg	314	314
Max. power (pressure management)	kW	25.2	25.2
Max. power (LH_2 pump)	kW	2.3	2.3
Parameter	**Unit**	**LH_2 distribution pipe**	**GH_2 venting pipe**
Max. mass flow	kg/s	0.33	0.02
Inner pipe outer diameter	mm	31.8	25.0
Inner pipe wall thickness	mm	2.6	2.0
Outer pipe outer diameter	mm	70.0	51.0
Outer pipe wall thickness	mm	2.9	2.6
Total length	m	76	20
Mass	kg	524	87
Length-specific mass	kg/m	6.9	4.3

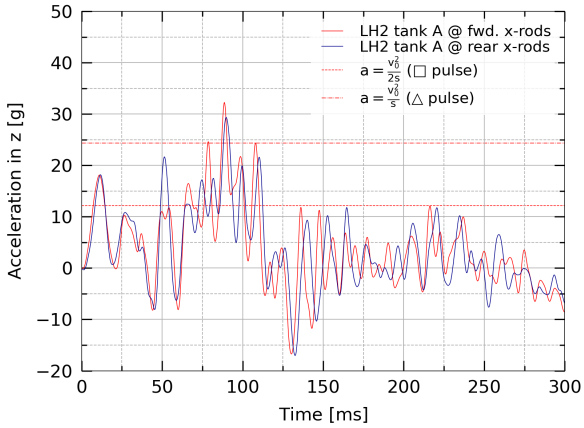
Table 9 – Results of the LH_2 supply system sizing process



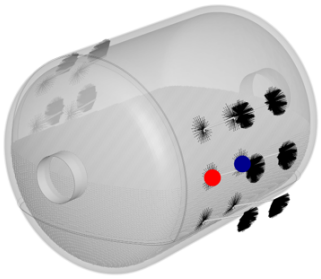
(a) Component level



(b) Major component level

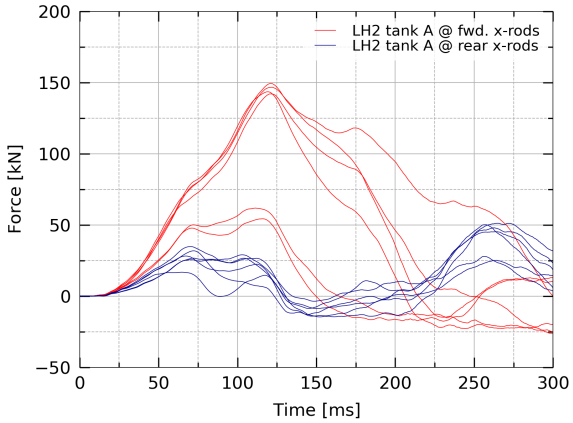


(c) Full-scale level

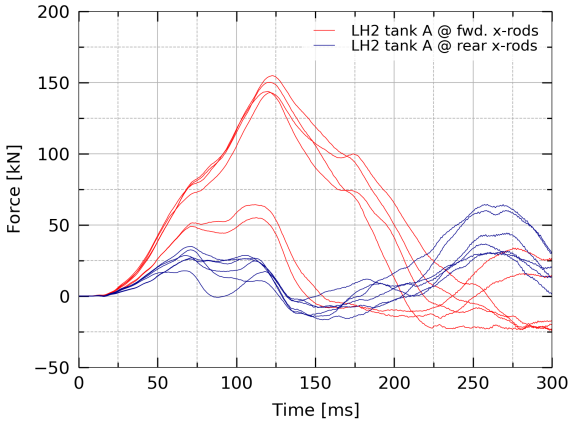


(d) Location of evaluation nodes

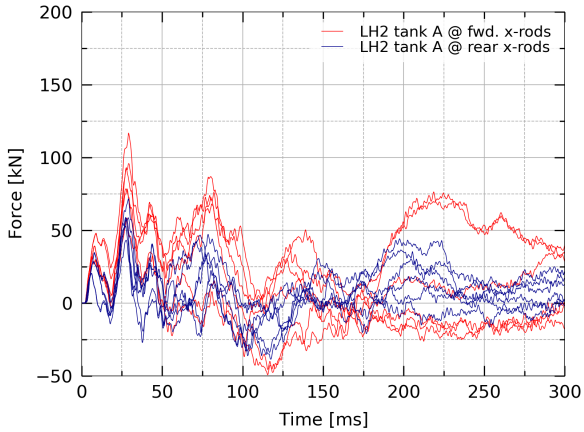
Figure 28 – Accelerations in z-direction at lateral tank surface (forward LH_2 tank)



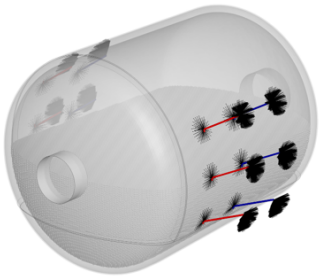
(a) Component level



(b) Major component level



(c) Full-scale level



(d) Location of evaluation x-rods

Figure 29 – Axial forces in the x-rods (forward LH_2 tank)